

SUBHOURLY PROFILING OF ATMOSPHERIC STABILITY
DURING SOUTHERN GREAT PLAINS SEVERE WEATHER EVENTS

by

Timothy J. Wagner

A thesis submitted in partial fulfillment of
the requirements for the degree of

MASTER OF SCIENCE
(Atmospheric and Oceanic Sciences)

at the

UNIVERSITY OF WISCONSIN-MADISON

2006

Approved:

Steven A. Ackerman,

Professor of Atmospheric and Oceanic Sciences

Date:

Abstract

Most studies of severe weather environments have focused only on synoptic time rawinsonde observations, thus preventing analysis of short-term stability trends. In this study, the enhanced temporal resolution of the combined Atmospheric Emitted Radiance Interferometer (AERI) and National Oceanic and Atmospheric Administration (NOAA) 404 MHz wind profiler observations allow for a unique analysis of stability changes near tornadic storms. From 1999 through 2003, AERI systems were collocated with NOAA wind profilers at five sites in the southern Great Plains of the United States, creating a large dataset of atmospheric soundings in both the pre-storm and post-storm environments. The radiance observations from AERI, a passive ground-based infrared radiometer with a resolution of better than 10 minutes, can be used to obtain temperature and moisture profiles through a physical retrieval process. NOAA wind profilers return actively-sensed wind profiles every six minutes.

Median values for eight standard severe weather indices were calculated for tornadic storms and non-tornadic supercells. Generally, instability increases throughout the day reaching a peak roughly an hour before a tornado forms or the non-tornadic supercell drops large hail. Wind shear, on the other hand, remains relatively constant throughout the pre-storm time.

In addition to climatologies of standard severe weather indices, case studies of tornadic events are presented to show how these observations can be applied to nowcasting.

Acknowledgments

This thesis represents the climax of one chapter of my life. Like a good book, my life has been blessed with a wonderful cast of characters. No one can truly accomplish anything without the support and care of others, and while some have helped mold me into a better research meteorologist, others have helped mold me into a better person.

Almost three years ago to the day, I arrived at the University of Wisconsin-Madison with a new diploma, some used furniture, and a bunch of trepidation. I didn't quite know into what I had gotten myself. I knew that I was interested in the workings of the atmosphere, but my interests weren't focused on any one specific area. Fortunately, Dr. Steve Ackerman and Wayne Feltz were these to show me that the world of remote sensing was full of fascinating possibilities. They provided the perfect balance between providing guidance without being overbearing, allowing me to progress along my own path to my own discoveries. They introduced me to the perfect project: one that blended something I was interested in (convection) with something I knew nothing about (passive remote sensing). I will appreciate the impact that Steve and Wayne have had on me throughout my career, even if Wayne now regrets making me a Matlab man. Dr. Michael Morgan and Dr. Greg Tripoli provided useful feedback and constructive criticism of this thesis; their input made this a better document.

I owe significant thanks to all the friends and family who helped me go this far. First off, my parents, Jim and Judy Wagner, deserve praise for continuing to patiently answer the

frequent question "your son isn't finished with college yet?" They always encouraged me to work harder, even when I thought I was working as hard as I could (I often wasn't). My family, along with my dear Bloomington friends Dan O'Neill and Hana Johnson, always make trips back to Indiana something to be enjoyed.

There were the friends who stuck with me through my undergraduate days and encouraged me to follow my graduate school dream even if it meant leaving Oklahoma: Cody Kirkpatrick, Leslie (Underwood) McCormick, Harold Peterson, Anne Przykucki, Judy Reilly, Michael and Maria Scaperlanda, and Donna Steele. I don't miss Oklahoma summers, but I do miss these people.

Madison isn't just where I live. It's my home. I feel that way thanks to the friendship of Marcella Colbert, Mark Kulie, Brent Maddux, Mark Marhol, Pedro Mulero, Everest Ong. and Nate Uhlenbrock. My officemates Richard Dworak, Jay Hoffman, and Yinghui Liu deserve praise for putting up with my restless pacing when numbers weren't crunching right. Shaima Nasiri shared much of her wisdom about being a graduate student with me. Robin Tanamachi wrote much of the original thermodynamic stability code used in this study. Maria Vaysis

Of course, special thanks go to Erin Hokanson. Over the past three years, she's shared in my happiness, cheered me when things were not going well, and was unafraid to tell me when I was just plain in the wrong. She is the best friend anyone could ask for. I can't wait for our next Amtrak adventure, whenever and wherever it may be.

Finally, thanks go to Madison itself. From great parks to beautiful lakes, Concerts on

the Square to excellent buses, Culver's to Lunchbox, I have enjoyed living here more than any other city (and I've lived in quite a few).

As I wrote in the beginning, this is the end of just one chapter in my life. I could write a whole thesis on the various adventures I've had and the people with whom I've shared those adventures. Frankly, some day I hope to do just that. But for now, I'll turn my attention to the next chapter that's just starting: getting a doctorate. There will be more trials ahead, there will be more joys. I don't all of what the next three or four years hold, but I do know that the people who have helped me thus far will still be right behind me. To each and every one of you, and to the ones I neglected to mention by name, thanks.

Tim Wagner
Madison, Wisconsin
August 2006



Non-tornadic supercell over the Ardmore, Oklahoma, railroad depot, about 100 km due south of the AERI and wind profiler installation in Purcell. This depot was shared by the Atchison, Topeka, & Santa Fe Railway and the Chicago, Rock Island, & Pacific Railroad, and is used today by Amtrak's *Heartland Flyer*. This photo combines two of the author's passions in one succinct picture: meteorology and American railroads. Photo by the author, Spring 2002.

Table of contents

Abstract	i
Acknowledgments	ii
Table of contents	v
List of figures	vi
List of tables	x
I. Introduction	1
II. Instability and its measures	6
A. Convection and indices	6
B. Past studies of indices	12
C. Unique attributes of this study	14
III. Instrument background	16
A. The Atmospheric Emitted Radiance Interferometer	16
B. Wind profilers	19
IV. Thermodynamic retrievals	22
A. An ill-posed problem	22
B. Retrieval techniques	25
C. The AERIPROF algorithm	26
V. Climatologies	30
A. Methodology	30
B. Tornado results	33
b1. Thermodynamic indices	34
b2. Shear indices	39
b3. Combined indices	41
C. Non-tornadic supercell results	43
c1. Thermodynamic indices	44
c2. Shear indices	48
c3. Combined indices	50
D. Changes	52

VI. Case studies	55
A. 8-9 May 2003	55
B. 18-19 September 2002	66
C. Comparisons	75
VII. Conclusions	76
References	79

List of figures

Figure 1.1: United States tornado fatality rate, 1950-2005.	3
Figure 3.1: An example of an AERI measured infrared spectrum.	17
Figure 3.2: Returned signal power for one of the three beams of a NPN radar wind profiler for 24 hours of observations.	20
Figure 4.1: Selected weighting functions for AERI.	28
Figure 5.1. Map of locations of tornadoes and non-tornadic storms used in this study, as well as the locations of the AERI observation sites.	32
Figure 5.2. Plot of the quartile values of Convective Available Potential Energy (CAPE) for all tornadic events in the SGP domain from eight hours before touchdown to three hours after touchdown as retrieved from AERI data.	35
Figure 5.3. As in Figure 5.2, but for Convective Inhibition (CIN).	36
Figure 5.4. As in Figure 5.2, but for Lifted Index (LI).	37
Figure 5.5. As in Figure 5.2, but for Showalter Index (SI).	38
Figure 5.6. Plot of the quartile values of Storm-relative Helicity (SRH) for all tornadic events in the SGP domain from eight hours before touchdown to three hours after touchdown as retrieved from NPN data.	39
Figure 5.7. As in Figure 5.6, but for Bulk Richardson Shear (BRN shear).	40
Figure 5.8. Plot of the quartile values of Energy-helicity Index (EHI) for all tornadic events in the SGP domain from eight hours before touchdown to three hours after touchdown as retrieved from AERI and NPN data.	41
Figure 5.9. As in Figure 5.8, but for Bulk Richardson Number (BRN).	42

Figure 5.10. Plot of the median values of CAPE for all tornadoes and all non-tornadic supercells in the SGP domain from eight hours before the event until three hours after.	44
Figure 5.11. As in Figure 5.10, but for CIN.	45
Figure 5.12. As in Figure 5.10, but for LI.	46
Figure 5.13. As in Figure 5.10, but for LI.	47
Figure 5.14. As in Figure 5.10, but for SRH.	48
Figure 5.15. As in Figure 5.10, but for BRN Shear.	49
Figure 5.16. As in Figure 5.10, but for EHI.	50
Figure 5.17. As in Figure 5.10, but for BRN.	51
Figure 5.18: Plots of a unitless change parameter for tornadoes and supercells for six indices from 8 hours before event formation to three hours after.	53
Figure 6.1: Map showing the location of tornadoes during the 8-9 May 2003 tornado outbreak.	56
Figure 6.2: Composite chart showing the synoptic conditions at 0000 UTC on 9 May 2003 (7:00 PM CDT, 8 May) over the central United States.	56
Figure 6.3: A time-height plot of water vapor mixing ratio at Vici, Oklahoma, and Hillsboro, Kansas, from 1400 UTC on 8 May to 100 UTC on 9 May 2003.	57
Figure 6.4: Visible geostationary satellite images centered over Wichita, Kansas, showing the evolution of the 8-9 May 2003 tornadic storms.	58
Figure 6.5: Plot of AERI-retrieved CAPE from 1400 UTC on 8 May 2003 through 100 UTC on 9 May 2003 for all AERI sites in the Southern Great Plains.	59

Figure 6.6: As in Figure 6.5, but for CIN.	60
Figure 6.7: As in Figure 6.5, but for LI.	60
Figure 6.8: As in Figure 6.5, but for SI.	61
Figure 6.9: As in Figure 6.5, but for SRH as measured by wind profiler.	63
Figure 6.10: As in Figure 6.5, but for BRN shear as measured by wind profiler.	63
Figure 6.11: As in Figure 6.5, but for EHI as measured by combined AERI and wind profiler observations.	64
Figure 6.12: As in Figure 6.5, but for BRN as measured by combined AERI and wind profiler observations.	65
Figure 6.13: Map of the locations of the two tornadoes during the storms of 18-19 September 2002.	66
Figure 6.14: Plot of surface conditions in south-central United States at 1900 UTC on 18 September 2002.	67
Figure 6.15: Visible geostationary satellite images centered over Wichita, Kansas, showing the evolution of the 18-19 September 2002 tornadic storms.	68
Figure 6.16: Plot of AERI-retrieved CAPE from 1500 UTC on 18 September 2002 through 200 UTC on 19 September 2002 for all AERI sites in the Southern Great Plains.	70
Figure 6.17: As in Figure 6.16, but for CIN.	70
Figure 6.18: As in Figure 6.16, but for LI.	71
Figure 6.19: As in Figure 6.16, but for SI.	71
Figure 6.20: As in Figure 6.16, but for SRH as measured by wind profiler.	73

Figure 6.21: As in Figure 6.16, but for BRN shear as measured by wind profiler.	73
Figure 6.22: As in Figure 6.16, but for EHI as measured by AERI and wind profiler.	74
Figure 6.23: As in Figure 6.16, but for BRN as measured by AERI and wind profiler.	74

List of Tables

Table 5.1: Table summarizing relevant values obtained in previous studies for tornadic, nontornadic supercell and severe weather (including both tornadic and non-tornadic storms).	34
--	----

I. Introduction

Severe weather has an undeniable societal impact. In an average year, severe thunderstorms, tornadoes, hail, and wind events combine for over 2.5 billion dollars in damages (Changnon and Hewings 2001). More important than financial loss is the toll on human lives. Because of these drastic effects on society, accurate and timely forecasting of severe weather events is imperative. While accurate forecasts are usually unable to prevent property damage by severe weather, these forecasts are literally lifesavers for those who find themselves in the path of severe weather. The earlier forecasts can be made and distributed to the general public, the earlier those affected by the severe weather can take appropriate action.

Tornadoes are a particularly significant threat in the United States. With winds often faster than 100 m s^{-1} , tornadoes are destructive and deadly. Since the year 2000, tornadoes have killed over 270 people in the United States (Storm Prediction Center 2005). Tornado development, climatology, and the discernment between tornadic and non-tornadic storms all remain active areas of research as new insights in these areas can help increase warning lead times and decrease false alarm rates.

A key part of severe weather forecasting is nowcasting, the process of forecasting for short time periods and specific locations. This includes predicting the movement and continuing development of existing storms as well as the immediate initiation of new ones. It is through nowcasting that the county-specific severe weather and tornado warnings are issued, which are extremely important to the general public as well as weather-dependent

industry like transportation and utilities (Wilson et al. 1998). The local forecast offices of the National Oceanic and Atmospheric Administration (NOAA) National Weather Service (NWS) are primarily responsible for nowcasting severe weather activity in the United States.

Short-term forecasting and nowcasting have been revolutionized by technological development. Innovations such as weather radar, satellite imagery, lightning detectors, and rapid-update forecast models have contributed to an ever-increasing trend of accuracy and lead-time in these predictions. Emergency management personnel and the general public have found value in these better forecasts. In the last century, the tornado fatality rate has dropped significantly, from 1.8 deaths per million people per year in 1925 to 0.12 deaths per million people per year in 2000 (Brooks and Doswell 2002). Since 1950, there is a decreasing trend in population-normalized tornado fatalities (Figure 1.1). A striking feature of this figure is that in recent years there are no major spikes and few minor ones in the fatality rate; most recent values are roughly the same magnitude as minima seen in earlier years. While the decrease in the tornado fatality rate cannot be entirely attributed to technological advances (as media proliferation and construction techniques are among the other factors responsible), the impact that these instruments have made on the forecasting process cannot be denied.

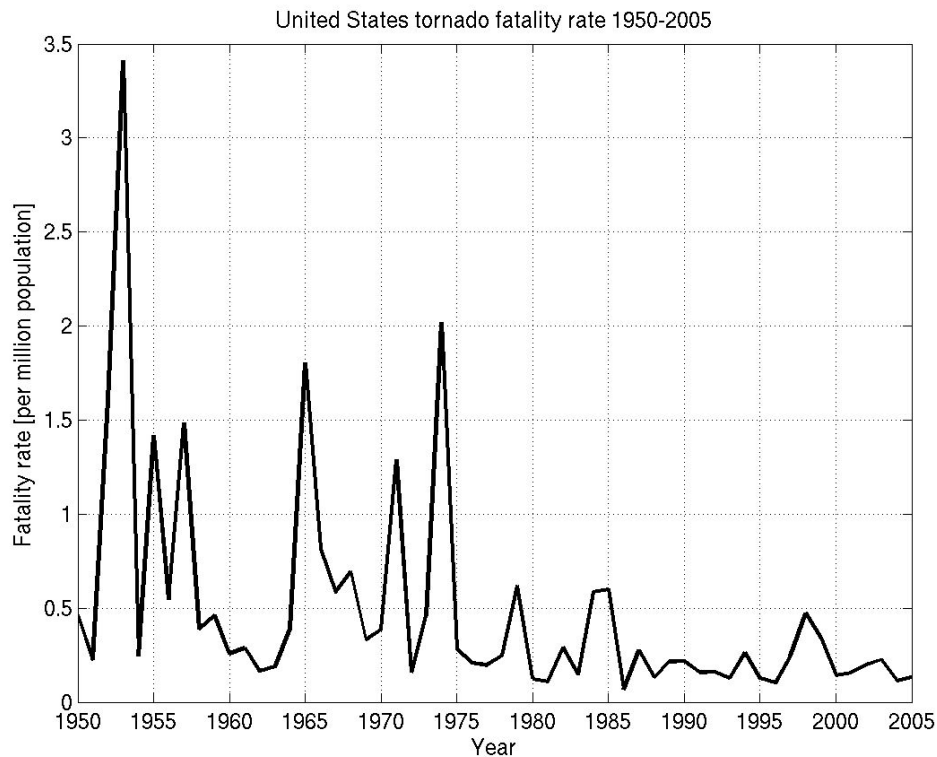


Figure 1.1: United States tornado fatality rate, 1950-2005. The rate is expressed in number of tornado fatalities per million population. Tornado fatality data obtained from the Storm Prediction Center. Population data 1950-1990 obtained from United States Census Bureau (1995). Population data 1991-2005 obtained from United States Census Bureau (2006).

The role of technological advances

Advances in meteorology are often fueled by improvements in the technology. More advanced instrumentation and measurement techniques can provide a forecaster with previously unavailable observations, further improving the accuracy and lead time of forecasts. Innovations can also advance the scientific investigation of severe weather, allowing for a greater understanding of the life cycle of severe convective storms and thereby fueling the development of next-generation models and instruments.

Upper-air observations are needed to accurately forecast many different types of

storms, but the spatial and temporal resolution of in situ upper-air observations is extremely coarse. These observations currently come primarily from radiosondes attached to lighter-than-air balloons. In the continental United States, radiosondes are launched from 90 locations at the synoptic hours of 0000 and 1200 UTC. The sparse distribution of launching sites and long gap between launches is a function of the expense associated with radiosondes: the instrument package is rarely reused and the launching process is mostly not automated. Since these instruments measure the entire depth of the troposphere, they are extremely important for assessing the stability of the atmosphere and its ability to support deep convection. The paucity of upper air observations means, as Moller (2001) writes, "accurately deducing the stability structure between sounding times is a formidable task."

Part of the gap in upper-air observations is being filled by the in situ observations from external aircraft sensors and transmitted to the surface via the Aircraft Communications Addressing and Reporting System (ACARS, Benjamin et al. 1991). However, few aircraft measure moisture and the diurnal cycle of air transportation means few observations are taken overnight. Satellites can also retrieve profiles of temperature and moisture. However, the large field of view of satellite sounders results in soundings measured over broad layers that are not necessarily representative of a single point (Menzel et. al 1998).

Since in situ observations of the upper atmosphere are expensive and rare, remote sensing becomes an attractive means by which quantitative data can be measured. Of particular interest are ground-based remote sensing instruments, which are ideally situated to capture variability near the surface, where it has the most impact on severe weather. The Atmospheric Emitted Radiance Interferometer (AERI), an instrument that can retrieve

temperature and moisture profiles of the lower atmosphere at less than ten-minute temporal resolution, shows promise as a useful nowcasting tool (Feltz et al. 2003, Feltz and Mecikalski 2002) . The National Oceanic and Atmospheric Administration (NOAA) Profiling Network (NPN, Chadwick and Hassel 1987), measures wind profiles at six minute resolution . Together, these two instrument networks can measure the same observations as radiosondes, but with a temporal resolution that is measured in minutes, not hours.

Uniqueness of this study

Occasionally a study has investigated stability indices generated from observations occurring more regularly than the standard synoptic times. For example, Davies (1993b) blended model forecast soundings with hourly surface observations to create more frequent observations of EHI. However, most climatologies of observed convective indices use a single observation per storm. The climatologies and benchmarks are created from these individual observations based on how far away and how recent the radiosonde was launched.

What separates this current study from these previous ones is the unique dataset that provides a high-temporal look at convective indices. By combining Atmospheric Emitted Radiance Interferometer (AERI) retrieved thermodynamic properties with wind profiler kinematic properties, many observations per storm can be identified. With all of these observations, stability trends and changes can be examined in detail.

II. Instability and its measures

A. Convection and indices

Many dangerous weather conditions are the result of the release of energy associated with the condensation of water vapor as moist parcels rise through the atmosphere (Doswell 2001). Parcels may initially be displaced upward through one of two processes: either the parcel is positively buoyant, or the parcel was lifted by an outside force as part of a large-scale ascent, like a cold front or flow over a mountain range. As air rises adiabatically and its pressure decreases, it cools. If the upward vertical displacement is sufficient, the parcels will cool to the point of condensation. From this level, ascending parcels will cool less slowly with altitude as the released latent heat from the condensation process will warm the parcel. The adiabatic lapse rate for parcels with uncondensed vapor is 9.8 K km^{-1} . For parcels in which condensation has occurred, the lapse rate depends on the moisture content of the parcel, and is about 6 K km^{-1} in the mid-troposphere.

The ability of the atmosphere to support parcel convection is known as instability. If the atmosphere cools at a faster rate with height than an ascending parcel, then once displaced parcels reach a level at which they are warmer than the environment, the parcels will continue to ascend without further forcing. Eventually, most parcels will stop rising once they rise to the altitude of the stratospheric inversion where stability is extremely strong. (A small percentage of parcels in large storms have enough vertical momentum to penetrate a short distance into the stratospheric inversion, creating the "overshooting top" characteristic of large cumulonimbus clouds.)

Convective indices are used as tools to help a forecaster ascertain the instability of the atmosphere. While older indices focused solely on finding a way to quickly quantify atmospheric instability, more recent indices have focused on other issues, such as discriminating between supercellular and non-supercellular storms. These indices are not intended to be stand-alone products nor are they expected to create perfect forecasts without human interpretation (Doswell 1996). However, they are capable of providing a snapshot of the basic atmospheric state at a geographic point, information that a forecaster can use in the process of predicting the type and severity of convection that will develop. An unusually large magnitude value of a particular index will serve notice to a forecaster to further investigate the situation and concentrate on a particular geographic area (Doswell 1994). Indices can also be used to compare the atmospheric environment on a given day to storm activity on previous days, so that a forecaster can judge the relative intensity and storm type of a prior event to current and future conditions.

The temperature, moisture, and wind profiles obtained from atmospheric profiles serve as the inputs for these indices. Initially, these data were obtained from rawinsonde launches. While these remain the standard source of convective index information, indices are frequently calculated from aircraft ascent and descent observations, numerical model output, and remotely-sensed data from satellites or ground-based instruments.

The first indices were created in the middle 20th century and were borne out of a desire to quickly assess atmospheric stability without resorting to the time-consuming process of plotting a sounding. During this early era, radiosonde observations were transmitted in numerical form via teletape instead of today's high-speed transmission

networks, and the mandatory pressure level data was broadcast well before the rest of the sounding. By reducing the sounding to a simple number plotted from the mandatory pressure level data, forecasters could quickly determine the instability present in the environment with a simple calculation or consultation of a chart instead of the laborious process of plotting the sounding on a pseudoadiabatic chart by hand.

The Showalter Index (Showalter 1953) was the first convective index in operational use. The Showalter Index (SI) is determined by first calculating the temperature of a parcel originating at 850 hPa that was lifted dry adiabatically to saturation and from there pseudo-adiabatically to 500 hPa. This temperature is then subtracted from the 500 hPa temperature to obtain the SI. If the resulting SI is negative, the index implies an unstable environment in which displaced parcels are warmer than their surroundings and therefore continue to rise. The more negative the number is, the more unstable the environment and the more likely that deep moist convection will develop.

Since the appearance of the SI, many subsequent indices have been developed as an aid to forecasting deep convection. One of the first to appear was the lifted index (Galway 1956), an index still in widespread use today. The lifted index (LI) is identical to the SI except for the definition of the displaced parcel, in which the condensation level is defined with respect to the mean mixing ratio of the lowest 900 m and the saturated adiabat of the theoretical maximum surface temperature. If the maximum has already been reached, then the mean potential temperature for the lowest 900 m is used. This parcel definition has two major advantages over the SI definition: the parcel is more representative of the lower troposphere than a parcel from an arbitrary height, and the parcel never originates below

ground as can happen with an 850 hPa parcel at higher altitude locations. The LI is far more prevalent than the SI in modern operational use, however both of these indices have a major limitation in that they are primarily calculated using surface characteristics and do not take into account the fine-scale vertical structure of the atmosphere.

Not all convective indices are purely empirical. Some of them are comprised of physical parameters that directly measure atmospheric characteristics. One of the most commonly used indices is the Convective Available Potential Energy (CAPE, Moncrieff and Green 1972). This is a measurement of the maximum buoyant energy per unit mass available to do work on a convective parcel by lifting it to higher elevations, and is defined by the following equation:

$$CAPE = \int_{p_{fc}}^{p_{el}} \frac{R}{P} (T_{parcel} - T_{env}) dp$$

where T_{parcel} is the temperature of the lifted parcel, T_{env} is the environment temperature, R is the universal gas constant, p_{fc} is the pressure of the level of free convection, and p_{el} is the pressure of the equilibrium level. Graphically, CAPE can be represented on a skew T/log P diagram as the area on a between the lifted parcel temperature and the environmental temperature bounded by the level of free convection and the equilibrium level. The larger the CAPE, the more unstable the air mass. As CAPE is a measure of buoyant energy, it has physically meaningful units of $J\ kg^{-1}$.

The previously mentioned indices are well-suited to the problem of forecasting the intensity and severity of ordinary air-mass thunderstorms which grow and die in

environments without wind shear. However, they do little to provide insight into storms that typically form tornadoes since they do not reflect the state of the wind field.

In the absence of vertical wind shear (the measure of the change of the wind vector with height) thunderstorms are short-lived. Once precipitation begins, it falls into the updraft. The updraft is neutralized by the downdraft associated with the precipitation and evaporatively cooled air. Once the storm loses its energy supply, it quickly dissipates.

With vertical wind shear present, storms can become more long-lived. A change in wind speed with height will cause a storm to vertically tilt, thereby allowing the precipitation and downdraft to remain separate of the updraft. Wind shear is also responsible for the origin of rotation in supercell thunderstorms, from which the majority of the tornadoes in the southern Great Plains are formed (Trapp et al. 2004). Vertical speed shear is associated with horizontal vorticity. The horizontal vorticity may be tilted upwards by the updraft (Klemp and Rotunno 1983). This vorticity can be amplified by many factors, including vertical directional shear, baroclinic vorticity generation as a result of cooler temperatures in the downdraft, and by stretching (Davies Jones et al. 2001). This intense vertical vorticity serves as the rotating core of the supercell; however, with too much shear the storm will not stay together as a cohesive system. The magnitude of shear required for persistent storms is to a degree dependent on the amount of thermodynamic instability.

Some indices have been developed that attempt to parameterize the necessary balance between instability and shear required to maintain persistent storms. The earliest such index is the Bulk Richardson Number (Weisman and Klemp 1982) or BRN, which is a ratio of CAPE to a wind shear parameter:

$$BRN = \frac{CAPE}{(\bar{u}_{6000} - \bar{u}_{500})^2}$$

where \bar{u}_{6000} is the weighted mean wind speed in the lowest 6000 m of the atmosphere and \bar{u}_{500} is the mean wind speed in the lowest 500 m of the atmosphere. The BRN is a dimensionless number because the units of CAPE (J kg^{-1}) and velocity squared ($\text{m}^2 \text{s}^{-2}$) are equivalent. Observations have typically associated supercell storms with having a BRN value between 10 and 45. If the BRN is smaller than that range, the storms tend to be "ripped apart" from the strong shear before rotation can develop; if the BRN is larger, the storms tend to pop up and rain into their own updrafts since there is little shear to support separate updrafts and downdrafts.

The Energy Helicity Index (EHI, Hart and Korotky 1991) has become an index frequently referred to by forecasters. Like the BRN, the EHI is a hybrid index that combines thermodynamics with a wind shear parameter. The index is defined as

$$EHI = \frac{CAPE \cdot SRH}{1.6 \cdot 10^5}$$

where SRH is the storm-relative helicity (Davies-Jones et al. 1990), a measure of wind shear and a commonly used index on its own:

$$SRH = \int_0^h \left[k \cdot (V - C) \times \frac{\partial V}{\partial z} \right] dz$$

where \mathbf{V} is the horizontal wind vector, \mathbf{C} is the mean storm motion vector, and h is the integration depth. Typically, helicity is computed for a 3 km depth, but sometimes for low-level applications, a 1 km depth is used instead. The EHI has been shown to have skill at

discriminating between tornadic and non-tornadic supercells (Rasmussen and Blanchard 1998).

B. Past studies of indices

Many studies have looked to create climatologies of tornadoes and other severe convective weather based on convective indices. There are two major sources of data for these studies: radiosonde observations and mesoscale numerical model output. Presented in this section is a brief discussion of several studies that have generated climatologies of convective indices. Quantitative values associated with these studies are tabulated in Table 5.1 on page 34 to facilitate comparison with the results of this study.

One of the first studies to compare multiple severe convective indices as a predictor of severe convective activity was done by David and Smith (1971). Of the few indices that had been developed by this time, net potential energy was considered to be the best predictor of convection. While similar to CAPE, this parameter is calculated from the surface to 100 hPa. However, the SI was considered to be the most useful for operational forecasting purposes since in this era the mandatory pressure level data was broadcast hours before the entire radiosonde observation. The SWEAT index (Miller 1972, a combined thermodynamic and kinematic index not considered here) was considered to be the best predictor of tornadoes, which is not surprising in that it was the only index of the study to include wind shear information. Schultz (1989) calculated indices from NWS radiosondes launched from Denver, Colorado, to come up with benchmark values of convective indices for significant

and severe weather within a radius of 150 km. Like David and Smith (1971), a buoyant potential energy parameter was considered to be the best predictor of significant weather (defined as 0.6 cm hail, 18 m s^{-1} winds, or 15 lightning strokes per 2000 km^2 in a 5-minute period), while SWEAT was the best predictor of severe weather (defined using the the National Weather Service criteria of 2 cm hail, 26 m s^{-1} winds, or a tornado).

Davies and Johns (1993) and Johns et al. (1993) shared a dataset to investigate thermodynamic and kinematic parameters associated with strong and violent tornadoes. For these studies, all tornado outbreaks between 1980 and 1990 with at least two tornadoes rated F2 or greater and 60 km apart were investigated. Also, all tornadoes rated F3 or greater were included in the dataset. To determine the values of the various indices, the radiosonde profiles were interpolated to the tornado position.

Davies (1993a) investigated indices in the Southern High Plains of the United States. This region is just to the west of the region investigated in the present study. The climate of this area, including the Texas panhandle and eastern New Mexico, is at a higher elevation than the Southern Great Plains and is typically warmer and drier than that area. Profiles were obtained from a blend of surface data and model data, as well as radiosonde launches. The study found that tornadic supercell days were typically found to have strong instability and moderate helicity. Non-tornadic supercell days had strong instability but weak helicity. Non-tornadic days with severe weather had weak helicity and only moderate instability.

Brooks et al. (1994) calculated CAPE and helicity for the National Weather Service radiosondes launched from Oklahoma City in order to investigate the differences between the

environments of all tornadic and nontornadic mesocyclones within 160 km of the launch point.

Rasmussen and Blanchard (1998) analyzed every 0000 UTC sounding with positive CAPE from the year 1992 in order to quantify benchmark values for various severe weather types. Those profiles that had a meteorological event within 400 km and $\pm 75^\circ$ of the boundary layer mean wind vector were assumed to be representative of the inflow of those events and were subsequently classified into one of three categories: tornadic, non-tornadic supercell, and ordinary thunderstorm. Only soundings launched between six hours before and three hours after the event were used.

Davies (2004) used RUC model profiles with positive CAPE associated with tornado-warned supercells to investigate the CIN and the pressure of significant profile levels (the level of free convection and the lifting condensation level) as tornado predictors.

C. Unique attributes of this study

Occasionally a study has investigated stability indices generated from observations occurring more regularly than the standard synoptic times. Davies (1993b) blended model forecast soundings with hourly surface observations to create more frequent observations of EHI. However, most climatologies of observed convective indices use a single observation per storm. The climatologies and benchmarks are created from these individual observations based on how far away and how recent the radiosonde was launched.

What separates this current study from these previous ones is the unique dataset that provides a high-temporal look at convective indices. By combining Atmospheric Emitted Radiance Interferometer (AERI) retrieved thermodynamic properties with wind profiler kinematic properties, many observations per storm can be identified. With all of these observations, stability trends and changes can be examined in detail.

III. Instrument background

A unique component of this study is the instrumentation used to obtain thermodynamic and kinematic soundings. AERI and wind profilers are separate instruments with unique approaches to measuring specific characteristics of the atmosphere.

A. The Atmospheric Emitted Radiance Interferometer

The Atmospheric Emitted Radiance Interferometer (AERI) is a passive ground-based infrared interferometer (Knuteson et al. 2004a, 2004b). AERI measures downwelling radiance from 3.3 to 18.2 μm with spectral resolution of better than 1 cm^{-1} and a temporal resolution of better than 10 minutes. It was created as part of the Department of Energy (DOE) Atmospheric Radiation Measurement (ARM) program (Stokes and Schwartz 1994). AERI is absolutely calibrated to an accuracy of better than 1% of ambient radiance using a calibration that is traceable to the National Institute of Standards and Technology.

The AERI optics design features a movable scan mirror that transitions between three viewing states in each observation cycle: upward sky view, an ambient temperature blackbody, and a hot blackbody set at a constant temperature of 333 K. The atmospheric observation is for three minutes per cycle, while each of the blackbody observations is for two minutes. The interferometer uses a sandwiched HgCdTe/InSb detector to measure radiance by splitting the incoming radiation beam onto separate moving mirrors, then recombining the reflected beams to read the interference pattern. The adjustment in the path length caused by the moving mirrors can create constructive or destructive interference once

recombined; the resulting interferogram is a combination of all the interference patterns at all wavelengths in the AERI-observed spectrum. By using a Fast Fourier Transform (FFT) on the interferogram, the spectrum can thus be measured. An example of an AERI-measured spectrum is shown in Figure 3.1.

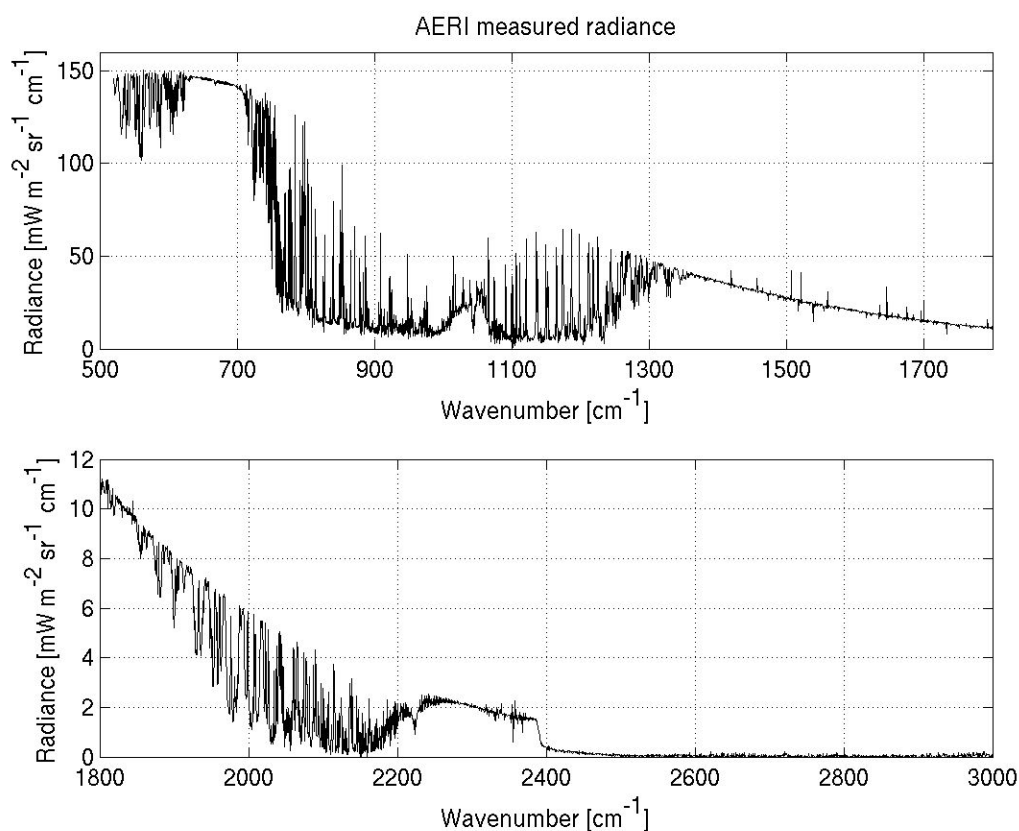


Figure 3.1: An example of an AERI measured infrared spectrum. Note the spectral resolution of 1 cm⁻¹. Because AERI is an upward-looking ground-based instrument, window channels have observations near zero and absorption lines point upwards for typical atmospheric conditions.

AERI measures a spectrum every two seconds in normal mode. By continually observing one of the three viewing states (hot blackbody, ambient blackbody, sky) for at least two minutes, many observations can be averaged together to reduce instrument noise. The

hot/ambient approach to instrument calibration assures high accuracy of the near-surface radiation as the detector is calibrated about the environmental temperature. If the ambient temperature is in excess of 313 K, the difference between the hot and ambient blackbodies is considered small and the observed radiances are flagged in the output file. AERI is also capable of a rapid-scan mode in which the transition between the three viewing states happens much more rapidly; downwelling radiance observations are taken at better than one-minute temporal resolution. This requires greater noise-reduction techniques, and none of these observations were used in this study.

AERI-observed radiances are converted into profiles of temperature and moisture in the lowest 3 km of the atmosphere through an iterative physical retrieval process (Smith et al. 1999, Feltz et al. 2005). This retrieval process is described in further detail in the following chapter.

AERI is automated and field-hardened and thus operates in a variety of conditions with minimal human interaction at the deployment site. Various incarnations of AERI have been deployed in environments as diverse as the stations in the arctic and ships in the tropics. Diagnostic conditions are monitored remotely, allowing real-time monitoring of not only the radiance observations but also the electrical, mechanical, and thermal conditions of all AERI instruments simultaneously.

To protect the AERI optics from precipitation, an automated hatch covers the viewing port whenever such conditions occur. While this prevents any radiance observations from being collected while precipitation is present, these observations are of little use in the thermodynamic retrievals.

B. Wind Profilers

Doppler radar can determine the motion of air currents by detecting the phase shift in the reflected electromagnetic pulse received by the radar antenna. Clear air Doppler radar does not require the presence of hydrometeors to obtain echoes, but instead receives reflected pulses from the gradients of turbulence. The ability of clear air Doppler to obtain quantitative observations of the wind field was first noted by Ecklund et al. (1979). A prototype network of automated radars dedicated solely to wind observation was installed in 1984 in eastern Colorado (Strauch et al. 1984), which served as a predecessor to the NOAA Profiler Network currently in use.

The NPN radars (Chadwick and Hassel 1987) operate at a frequency of 404.37 MHz, using a fixed phased-array coaxial-colinear grid antenna. Each radar generates three beams: one pointing vertically and beams pointing north and east at an elevation angle of 73.7° . Both the frequency and the elevation angle are a compromise between competing benefits (Doviak and Zrnich 1993, Strauch et al. 1984). The maximum altitude of a wind profiler observation is inversely proportional to its frequency so lower frequencies sense to higher altitudes. However, lower frequency radars require larger antennae, thereby increasing the expense. Lower frequencies also have longer receiver recovery times and larger pulse widths, which limit the minimum range of observation. High elevation angles insure that the three beams are looking at a small uniform volume, but low elevation angles result in more accurate horizontal wind components.

The radar profiler samples in two modes: low altitude and high altitude mode (van de Kamp 1988). The difference between the two modes is the length of the radar pulse; longer pulse lengths are used for higher altitude observations. This longer pulse length results in more power for higher altitudes observations at the expense of vertical resolution. The boundary between low and high mode is at 7.5 km above ground level. The vertical resolution for low-mode observations is 250 m. Since no observations above 6 km were required for this study, all observations used herein were from the low mode.

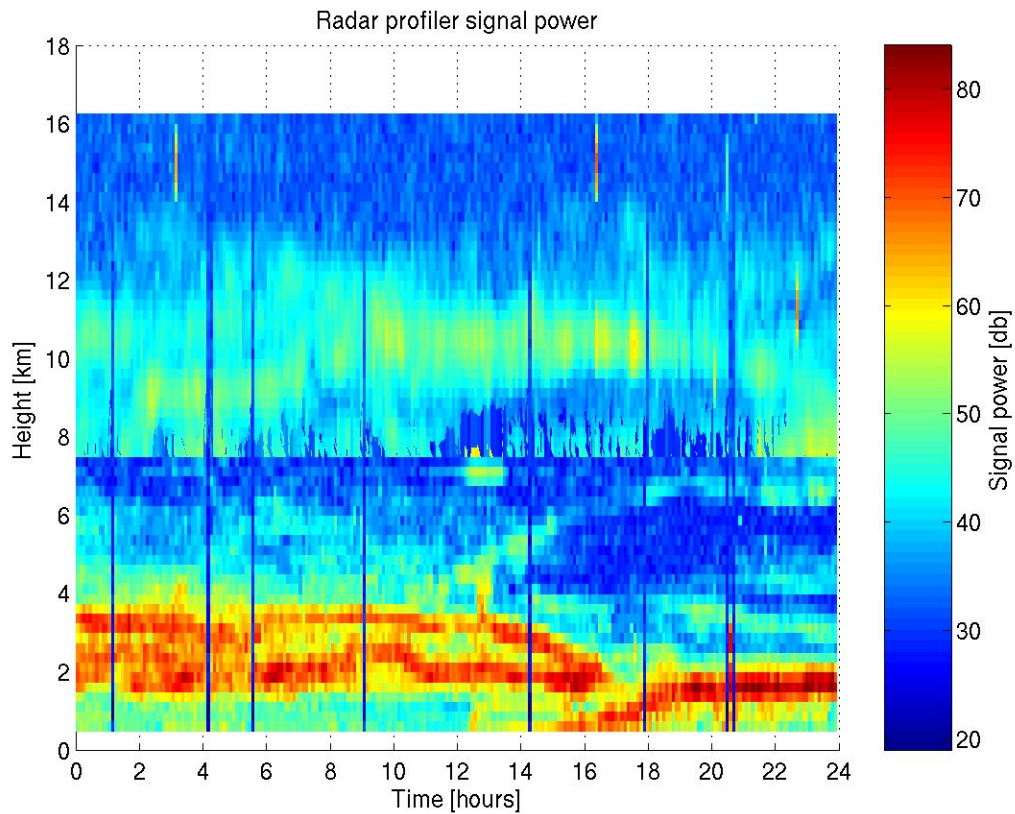


Figure 3.2: Returned signal power for one of the three beams of a NPN radar wind profiler for 24 hours of observations. The discontinuity in the returned signal at 7.5 km above the surface denotes the boundary between low-altitude mode and high-altitude mode.

NPN observations are taken every six minutes. As with AERI dwell time, this allows for frequent observations while allowing enough time at each observation for averaging to reduce noise. Rawinsonde observations show good agreement with collocated rawinsonde observations (Bedka et al. 2006). Data from the NPN is distributed in near real-time to forecasting agencies. Recent work has shown that the assimilation of NPN data leads to greater skill in short-term numerical weather prediction models (Benjamin et al. 2004).

IV. Thermodynamic Retrievals

In a hyperspectral observation of certain absorption bands in the atmosphere, enough information is contained in the measured spectrum to retrieve profiles of temperature and moisture. This inverse problem, however, is difficult as many temperature and moisture profiles can simultaneously satisfy a radiance measurement within a specified degree of tolerance. Sophisticated techniques must be used to retrieve this thermodynamic information in an accurate manner. In this section, an overview of the science of inverse retrieval is presented followed by a discussion of specific attributes of the AERIPROF algorithm used to retrieve profiles from AERI observations.

A. An ill-posed problem

All matter emits electromagnetic radiation as a function of its temperature. The total amount of emitted radiation and the wavelength of maximum emission are both temperature dependent: hotter substances emit more radiation and peak in shorter wavelengths. The maximum possible radiance at a given wavelength emitted from a substance with a given temperature is described by the Planck function:

$$B_{\lambda}(T) = \frac{2hc^2}{\lambda^5(e^{hc/k_B T} - 1)}$$

where T is the temperature of the substance, λ is the wavelength of interest, $c = 2.998 \times 10^8$ m s⁻¹ is the speed of light, $h = 6.626 \times 10^{-34}$ J s is the Planck constant, and $k_B = 1.381$ J K⁻¹ is the Boltzmann constant.

When looking through the atmosphere, the Planck function is not sufficient to describe the incident radiation on an instrument, as the atmosphere emits and absorbs radiation. The optical depth, τ , of a layer is a representation of the attenuation in that layer such that:

$$I_2 = I_1 e^{-\tau}$$

where I_1 is the radiance entering the layer and I_2 is the radiance leaving the layer, neglecting emission of the layer itself. For a real τ , the value of $e^{-\tau}$ will be between zero and one. This fraction of radiance transmitted, or transmittance, depends on the wavelength of interest and the gases present in the layer. Certain wavelengths can pass through the atmosphere relatively unimpeded. For example, the visible portion of the spectrum is little affected by clear air. Other wavelengths, like the 9.6 μm ozone absorption band, are completely blocked by the constituent gases of the atmosphere. The change in transmittance with respect to height is known as the weighting function, W .

The total amount of radiation measured at the surface by an upward-looking instrument is equal to the background radiation attenuated over the total depth of the atmosphere plus the emission and absorption of each atmospheric layer summed over the total atmospheric depth. These relations form the downwelling radiative transfer equation:

$$I_\lambda(0) = I_\lambda(\infty) e^{-\tau} + \int_0^\infty B[T(z)] W(z) dz$$

where $I_\lambda(0)$ is the radiation observed at the surface, $I_\lambda(\infty)$ is the cosmic background radiation (which is negligible for infrared wavelengths), and z is the altitude of a layer. The process of physical temperature profile retrieval consists of inverting the above equation so that the

temperature profile $T(z)$ satisfies the observed $I_\lambda(0)$ for all wavelengths. Moisture retrieval finds the proper distribution of moisture by retrieving the vertical profile of absorption in parts of the spectrum where water vapor is highly absorbing.

Carbon dioxide, CO_2 , is commonly used as a sounding gas for temperature because it exists at a constant mixing ratio at all altitudes. When measuring at a wavelength close to the center of a CO_2 absorbing channel, the radiance measured will have originated from very near the sensor because the atmosphere is opaque to such a wavelength. An upward-looking surface-based sensor will measure a high the radiance and retrieved temperature for such a case. As the sensor looks at nearby wavelengths, the reduced opacity means that the measured radiance includes contributions from higher in the atmosphere. If the measurement is taken at one of the so-called window channels where atmospheric opacity is very low, the sensor will register very low radiances because it is sensing to the very highest reaches of the atmosphere and outer space.

Alas, weighting functions are broad, overlapping curves and so a single radiance observation will contain information from many different levels of the atmosphere. This leads to many possible thermal profile solutions for a spectrum. Even though a retrieved profile may properly satisfy the measured radiances, this profile could be an entirely incorrect representation of the true atmospheric state (Rodgers 2000). Because of this, techniques have been developed to better pinpoint the distribution of temperature and moisture that would generate a given observed spectrum. Statistical retrieval and physical retrieval are techniques that are both important to AERI thermodynamic retrieval, and they are described below.

B. Retrieval techniques

One method of retrieving thermodynamic profiles from observed radiance spectra is through a statistical retrieval (Feltz et al. 1998). Instead of inverting the radiative transfer equation to solve for a profile satisfying the observed radiances, the statistical retrieval compares observed radiances with known radiances calculated from previous profiles.

Forward radiative transfer models are computer models that take input profiles of temperature and gas mixing ratios and calculate what the observed radiance would be in such an environment. If many radiosondes representing a variety of meteorological conditions are launched and the resulting profiles are processed through a forward model, then a large database of radiance spectra associated with known atmospheric profiles is created. When an instrument observes a radiance spectrum, regression techniques can use the observed radiances to obtain a likely profile (Smith et al. 1999, Feltz et al. 1998).

While the statistical technique is simple, it is not robust. If the environmental profile is sufficiently different from previous radiosonde observations, the solution will not be accurate. Should an instrument be deployed in a data-sparse environment, a purely statistical retrieval will not work as no profiles exist to which observed spectra can be compared.

Physical retrieval addresses these concerns by inverting the radiative transfer equation to find a profile that optimally matches the observed radiances. A first-guess profile is run through a forward radiative transfer model to calculate radiances. The calculated values are compared with the observed values, and then the first-guess is adjusted, starting from the surface and working to the top of the atmosphere. The resulting profile is processed back

through the forward model. This process is continued iteratively until the calculated and observed radiances are within a specified tolerance of each other. Smith (1970) was the first to propose an iterative technique that did not assume a set number of layers, meaning that a physical retrieval could more accurately capture the vertical variability inherent in the near-surface levels of the atmosphere.

The first guess is necessary in that it constrains the final solution to a likely answer. Since temperature retrieval requires an absorbing gas profile (including water vapor) and moisture retrieval requires a temperature profile, these assumed profiles are important starting points. In the upper levels of the atmosphere, where there is little information about the profile contained in the observed radiances, the first-guess profile insures that the retrieved result resembles the environmental state.

C. The AERIPROF algorithm

The AERIPROF algorithm (Feltz et al. 2005) is a UNIX-based series of FORTRAN routines that uses a physical retrieval to obtain the thermodynamic profiles from AERI observed radiances. It was developed at the Space Science and Engineering Center (SSEC) with preliminary work starting as far back as 1989.

As previously stated, a valid first guess is an important part of any physical retrieval. Prior incarnations of the AERI retrieval algorithm obtained first guess profiles of temperature and moisture from either purely statistical sounding regressions or from GOES sounder retrievals blended with those regressions (Feltz et al. 2003). The current algorithm uses a

blend of the Rapid Update Cycle 2 (RUC-2) numerical weather prediction model (Benjamin et al, 1998) and statical regressions (Feltz et al. 2003). RUC-2 assimilates observations from surface stations, aircraft, wind profilers, satellites, rawinsondes, and other sources to create its analysis and forecasts every hour. The RUC-2 analysis was chosen over GOES retrievals because these retrievals are only possible in clear-sky conditions. The RUC-2 four-dimensional gridded data is interpolated in time and space to create a rough profile of the atmosphere over the AERI instrument location at the observation time, and it is blended with the statistical regression in the lower atmosphere where the coarser vertical resolution of the RUC-2 is unable to properly capture phenomena like inversions.

This first guess is then processed through a forward radiative transfer model along with in situ surface measurements to convert the temperature and moisture profiles into appropriate spectra, which are then compared to the AERI observation (Feltz et al. 2003). The temperature retrieval uses measurements found between 610 to 720 cm^{-1} (13.9 to $16.4\text{ }\mu\text{m}$) and 2223 to 2260 cm^{-1} (4.4 to $4.5\text{ }\mu\text{m}$), where CO_2 strongly absorbs. The water vapor retrieval uses the observations from the 538 - 588 and 1250 - 1350 cm^{-1} (17.0 - 18.6 and 7.4 - $8.0\text{ }\mu\text{m}$) spectral regions. From these measurements, the temperature and moisture profiles are adjusted iteratively to minimize the difference between the modeled and observed radiance until the resulting profiles have radiance measurements within a specified tolerance of the AERI observation. To verify that the sky is cloud free, observations from a collocated laser ceilometer are also ingested into the algorithm. AERI retrieved profiles have been shown to

have good agreement with rawinsonde thermodynamic profile and stability observations (Feltz et al. 2003, Feltz and Mecikalski 2002, Turner et al. 2000).

The weighting functions peak near the surface where density of the atmosphere is the greatest (Figure 6.1). Because of this, AERI profiles have the best vertical resolution at low altitudes. While this means that the best vertical resolution is where the greatest variability instability occurs, the downside is that there is little information in the AERI-measured radiance above 3 km. The output retrievals above 3 km in altitude consist almost entirely of the first-guess RUC-2 data.

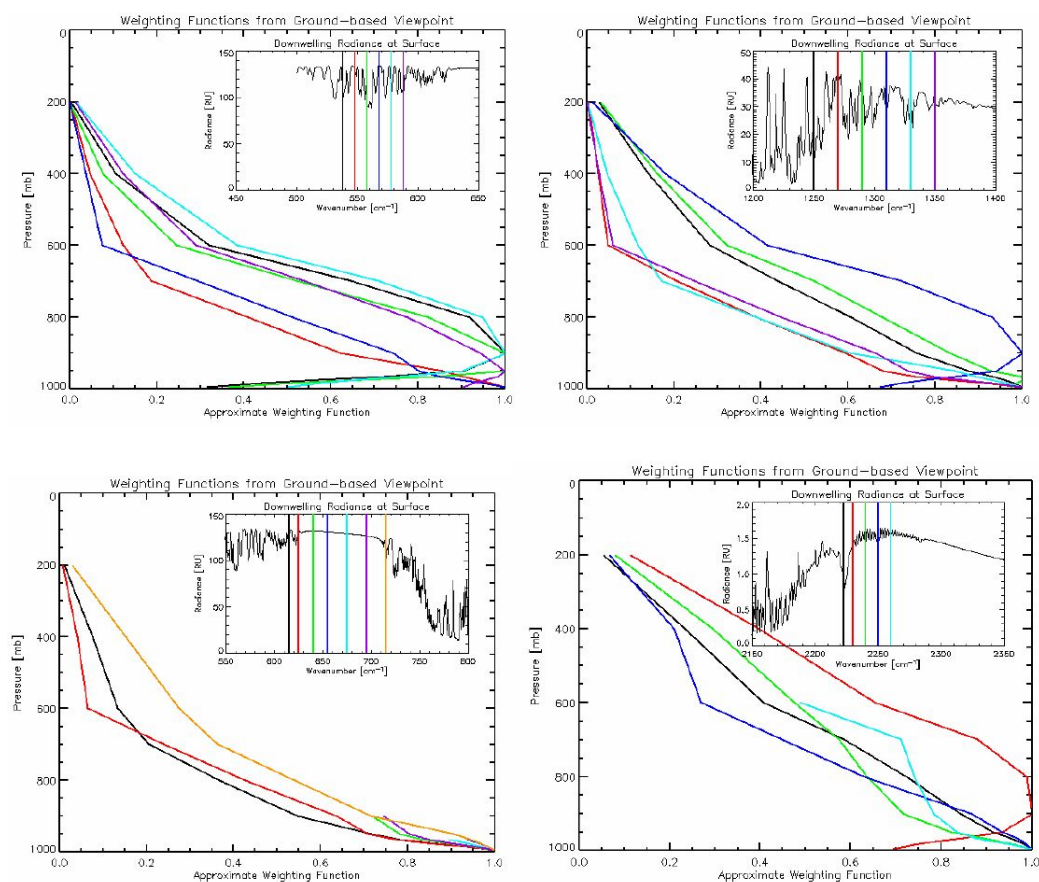


Figure 4.1: Selected weighting functions for AERI. The spectral region of each weighting function is shown in the upper-right corner of each panel. The top two panels show weighting functions in spectral regions used for vapor retrieval; the bottom two panels show weighting functions in temperature retrieval regions. From Feltz et al. (2005).

For this study, all five years of ARM-SGP AERI retrievals were reprocessed from the original constituent data. While the AERI system executes retrievals in real-time, this does not include independent quality control checks on the AERI observations or any of the other data required for retrieval. Therefore, it was decided to reprocess all retrievals using the quality-controlled data available from ARM. This dataset covering all five SGP facilities from 1999-2003 is now available for use in other studies.

V. Climatologies

The value of AERI and NPN observations is evident when used to determine characteristics of the atmosphere as severe weather events develop. As part of this, climatologies of convective indices were generated utilizing the high-temporal resolution observations of these ground-based profilers. The methodology and results are described in this section.

A. Methodology

From 1999 through the end of 2003, AERIs were located at five sites in Oklahoma and Kansas. Four of these sites are also home to NPN radar wind profilers. The fifth AERI site, Morris, Oklahoma, was located twenty kilometers from a NPN profiler in Haskell, Oklahoma. These two instruments were considered to be in the same location for the purposes of this study. A map of the AERI domain is seen in Figure 5.1. Throughout this time, these instruments were taking near-continuous observations of thermodynamic and wind profiles of the atmosphere through a variety of weather conditions.

To determine the time and location of severe weather events, the SeverePlot database (Hart 1993) was used. NOAA's Storm Prediction Center (SPC) produced and maintains this database of tornadoes, severe wind, and severe hail, accessible through a graphical interface. SeverePlot includes time, date, latitude, longitude, and magnitude of these severe weather events.

The experiment domain consists of all space within 100 km radius of at least one AERI site. This distance was chosen as it covered most gaps between AERI locations

without large overlaps. The SeverePlot database was then used to find all tornadoes that initially touched down within the experiment domain. Tornadoes forming within six hours of another tornado in the domain were deleted to remove the influence of repeat signals; if treated separately, two tornadoes occurring in range of the same observation site within a short time span would return almost identical observations and improperly affect statistics.

Stability indices were calculated for the remaining tornadic events. Since the time between AERI observations varies through the duration of the experiment, it was necessary to interpolate the values of the indices to a common time grid. Indices calculated from wind observations were also interpolated to that same grid so that ratios between thermodynamic and kinematic observations could be easily calculated. All indices for a particular tornadic event were calculated from the closest observation site to a storm's initial position.

This study also investigates AERI observations of non-tornadic supercells. Since the SeverePlot database does not contain a list of these storms, such a dataset had to be created from other observations. Rasmussen and Blanchard (1998) assumed that hail of two inches (5 cm) in diameter or larger served as a proxy for supercells since the buoyant force required to support hailstones of that size would likely come from the rotating updrafts characteristic of supercells. This definition was modified to include a temporal component separating non-tornadic storms from tornadic ones. For this study, a non-tornadic supercell was considered to be a storm that produced hail of two inches or larger and was separated from a tornado by more than 6 hours. The same criteria for deleting multiple tornadoes was used for supercells, and thenceforth the same procedures for index calculation and interpolation were used.

These procedures resulted in 53 tornadic events and 21 non-tornadic events used as the basis for this study. The locations of these storms relative to the observation sites is shown in Figure 5.1.

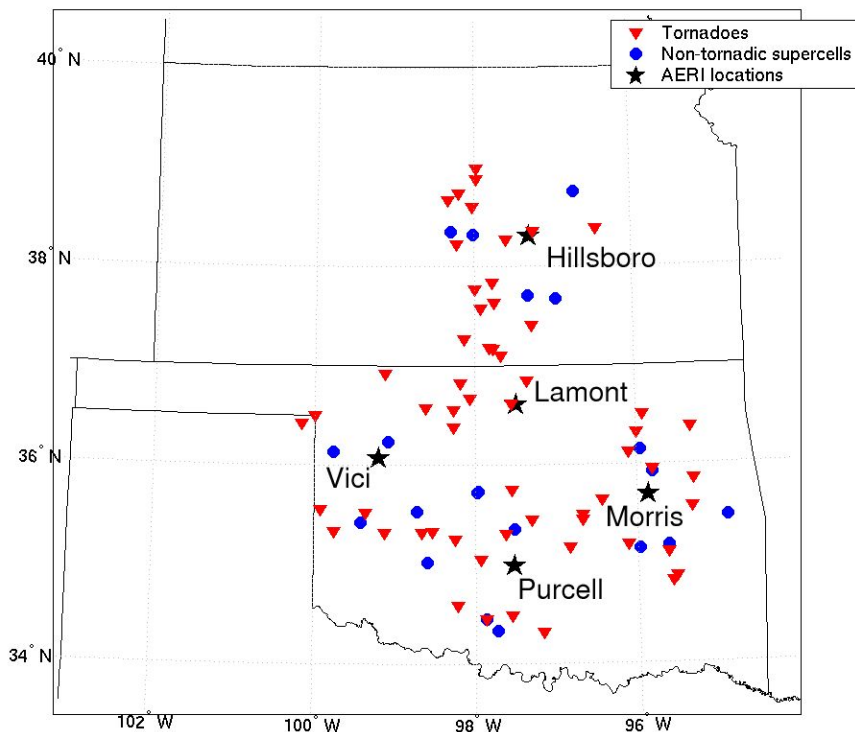


Figure 5.1: Map of locations of tornadoes (red triangles) and non-tornadic storms (blue circles) used in this study, as well as the locations of the AERI observation sites (black stars).

As previously noted, these observations are not always continuous. The AERIPROF algorithm will reject observations when low clouds are present and AERI automatically closes its hatch when precipitation is present. AERIPROF can output the RUC-2 profile interpolated to standard AERI observation levels when a direct retrieval is not possible. These data values were not used in this study.

Since supercells form discretely and individually rather than as part of a larger cloud mass, the inability of AERI to observe during low clouds and precipitation is not a significant liability. The majority of tornadoes in the southern Great Plains form from individual cells, as less than 25% of tornado days in Oklahoma and Kansas are due to quasi-linear convective systems (Trapp et al. 2005).

B. Tornado results

To view the pre-storm and post-storm environment, all indices are plotted from eight hours before to three hours after the tornado time as recorded in the SeverePlot database. The three quartiles (25th percentile, median, and 75th percentile) are shown. To calculate these statistics, all observations were resampled onto a 15-minute gridspace and smoothed using a running 1-3-1 filter. Due to the fact that some convective indices denote greater instability with larger positive numbers while other indices use more negative numbers, the quartile corresponding with larger values of instability is not always the third quartile. The following figures are grouped by index type: thermodynamic, kinematic, and combined. Discussions of values obtained from rawinsonde or model-based studies are included. To facilitate comparison, these values are summarized in Table 5.1 along with the relevant values for non-tornadic supercells.

	<i>RB98</i>	<i>D93a</i>	<i>D93b</i>	<i>D2004</i>	<i>RB98</i>	<i>D93a</i>	<i>D2004</i>	<i>S89</i>
type	Torn	Torn	Torn	Torn	Supr	Supr	Super	Severe
value	median	mean	mean	median	median	mean	median	mean
CAPE	1314	1895	2661		1152	1200		1900
CIN	12			31-38	35		72	
LI		-5.9	-7.6			-3.2		-5.29
SRH	180	304	151		124	160		
EHI	1.48	3.6	2.5		0.64	1.2		
BRN	7.5		42		6.6			

Table 5.1: Table summarizing relevant values obtained in previous studies for tornadic (Torn), nontornadic supercell (Supr), and severe weather (Severe, including both tornadic and non-tornadic storms). The studies are Rasmussen and Blanchard (1998, RB98), Davies (1993a, D93a), Davies (1993b, D93b), Davies (2004, D2004), and Schultz (1989, S89). Since some studies reported mean values, and other studies reported median values, the parameter type is also noted.

b1. Thermodynamic indices

Thermodynamic indices are obtained from the temperature and moisture profiles of the environment. Therefore, the measurements used in the following indices come solely from AERI with no input from NPN.

The plot of the median value of Convective Available Potential Energy (CAPE, Figure 5.2) shows that as time progresses, instability increases until about an hour before tornado touchdown. Instability then decreases with time. This trend is also seen in the first and third quartiles, but with a peak time occurring earlier. The values for CAPE match up favorably with Rasmussen and Blanchard (1998, hereafter RB98) which found a median value of 1314 J kg^{-1} for tornadoes. Davies (1993a, hereafter D93a) found a larger mean CAPE for tornadic storms at 1895 J kg^{-1} . Davies (1993b, hereafter D93b) found an even larger mean CAPE of 2661 J kg^{-1} for seven selected storms. Schultz (1989, hereafter

S89) found a median CAPE for severe weather in the Colorado plains (including tornadoes and large hail) to be 1900 J kg^{-1} . This disparity between S89 and the other studies could be due to the increased elevation of the surface in the S89 domain.

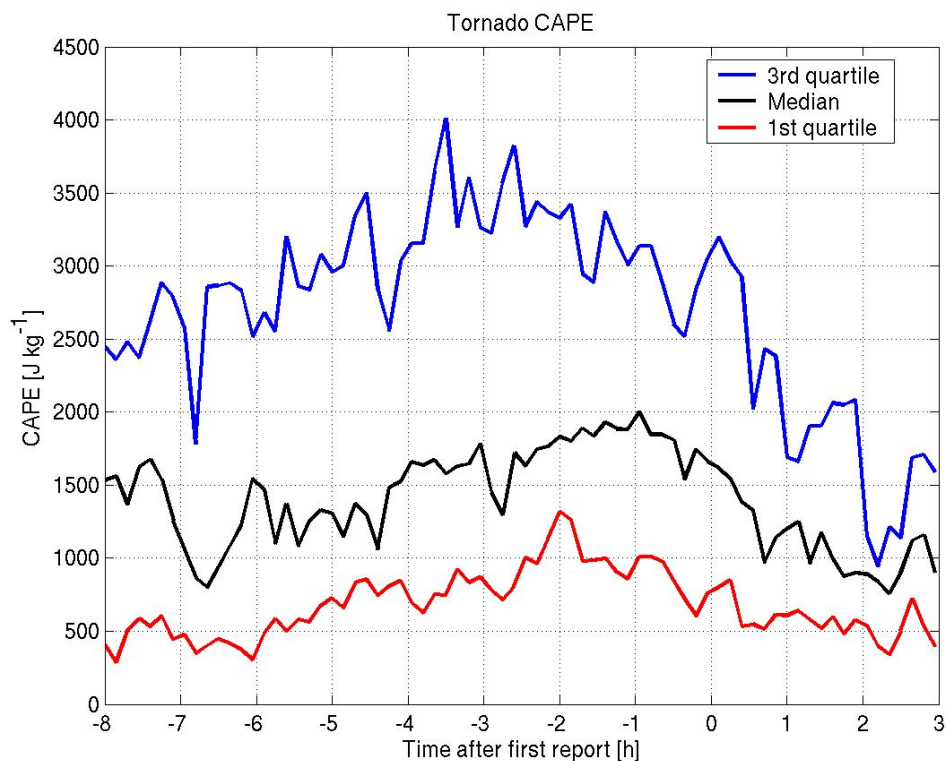


Figure 5.2: Plot of the quartile values of Convective Available Potential Energy (CAPE) for all tornadic events in the SGP domain from eight hours before touchdown to three hours after touchdown as retrieved from AERI data. The first quartile is denoted in red, the median in black, and the third quartile in blue.

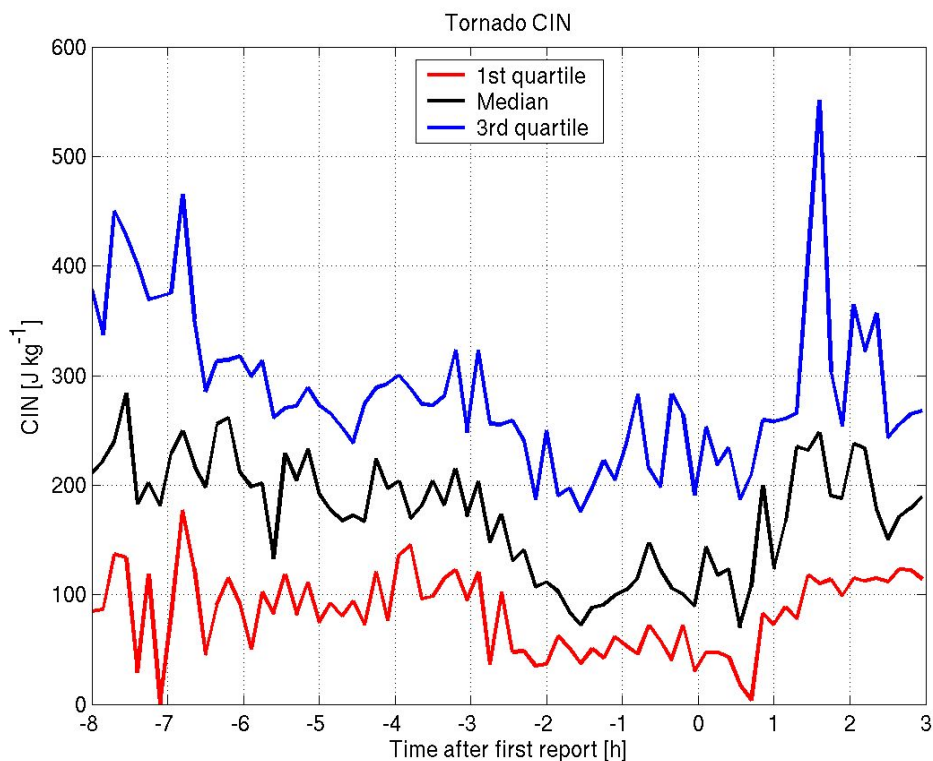


Figure 5.3: As in Figure 5.2, but for Convective Inhibition (CIN).

Convective Inhibition (CIN, Figure 5.3) shows an expected trend when compared to CAPE. Whereas CAPE generally increases as the time of tornadogenesis approaches, CIN decreases until about 1.5 hours before tornado touchdown, at which point it begins increasing. Case studies (as presented in chapter 6) show that convective initiation tends to follow a rapid decrease of CIN. This does not appear in the climatology as the time of this decrease relative to initiation can vary; averaging has smoothed out this signal.

The CIN values obtained from AERI are much larger than values found from rawinsonde-based studies. RB98 found a median CIN for tornado-producing storms of 12 J kg⁻¹, and Davies (2004) found a median mixed-layer CIN (generally larger than surface-based

CIN) of 38 for weak tornadoes (F0 and F1) and 31 for strong tornadoes (F2 and greater). The large values of CIN obtained by AERI when compared to other studies are likely due to the dependence of the calculation of CIN on the vertical resolution of the observed profile. Since AERI has a coarser vertical resolution than rawinsondes, the small variations in the profile are lost. However, the measured quantities are still valid insofar as trend analysis goes.

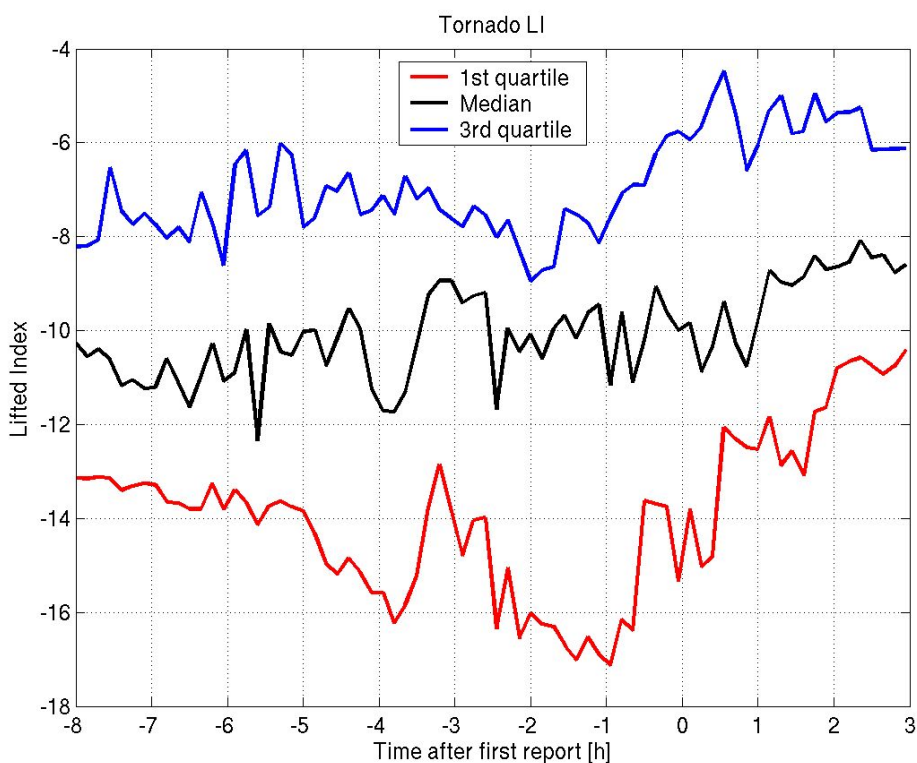


Figure 5.4: As in Figure 5.2, but for Lifted Index (LI).

Lifted Index (LI, Figure 5.4) clearly shows similar instability trends in the first and third quartiles. It is more difficult to discern such a trend in the median. This could be due to the fact that peaks in LI occurred at different times for different storms. The AERI-

retrieved LI values show a greater instability than those obtained from other rawinsonde studies: D93a found mean tornado LI to be -5.9, D93b found a mean of -7.6, and S89 found a median of -5.29.

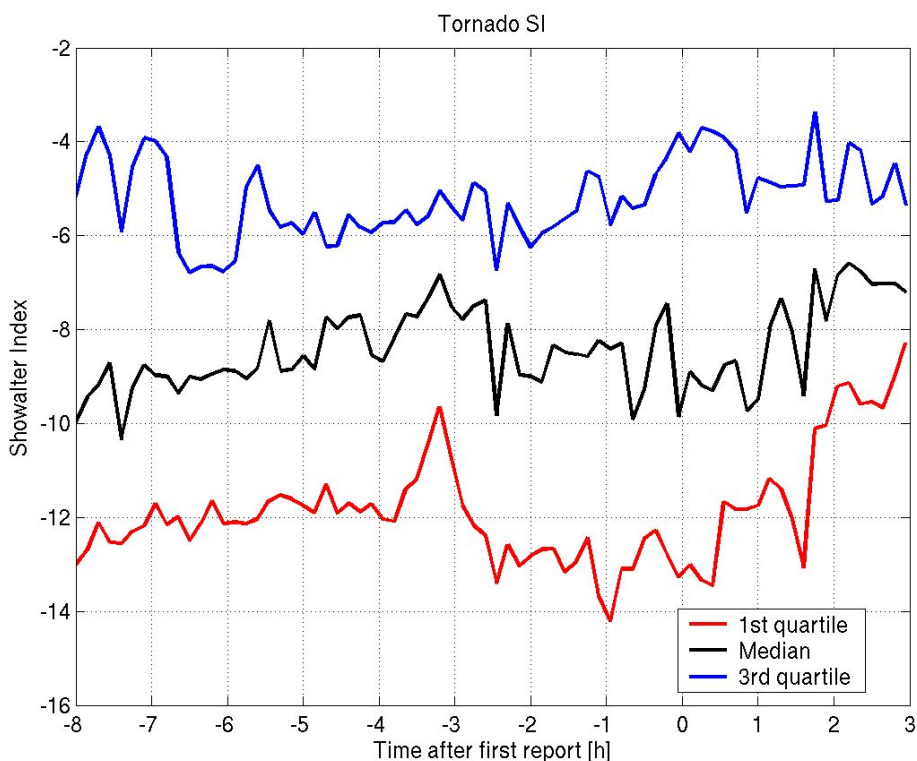


Figure 5.5: As in Figure 5.2, but for Showalter Index (SI).

While the Showalter Index (SI) is similar to the LI, the trends for the quartile values are somewhat different (Figure 5.5). The SI appears to become less negative with time until four or five hours before tornado formation, then it becomes more negative until the time of the tornado. After that, it once again becomes more stable. The different definition of ascending parcel for SI versus LI means that LI is able to more accurately capture the

influence of low-level moisture on deep convection and therefore plots of LI will show more variability when compared to SI.

b2. Shear indices

Since shear is a measure of the change in wind with height, only observations of the vertical wind profile are necessary to calculate the indices that measure shear. Therefore, the following two plots use only NPN observations in the calculations.

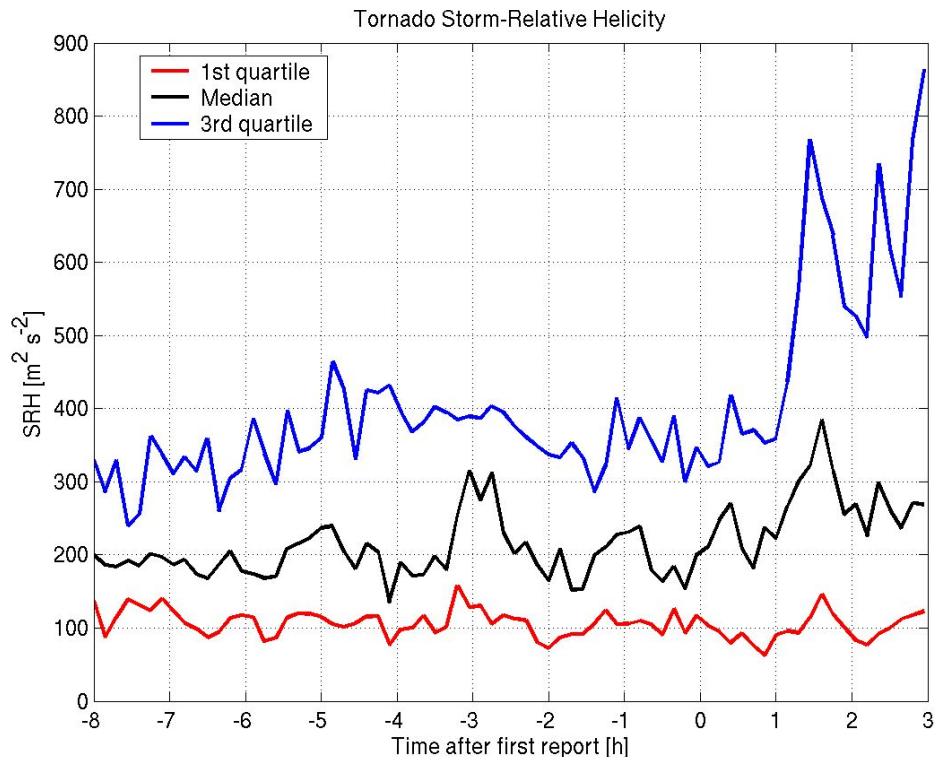


Figure 5.6: Plot of the quartile values of Storm-relative Helicity (SRH) for all tornadic events in the SGP domain from eight hours before touchdown to three hours after touchdown as retrieved from NPN data. The first quartile is denoted in red, the median in black, and the third quartile in blue.

Storm-relative Helicity (SRH, Figure 5.6) is fairly constant throughout the pre-storm environment. (All helicity values used in this study are from 0-3 km above the surface.)

Following the storm, it tends to increase. A large array of tornadic values of helicity can be

found in the literature. D93b found a mean value for SRH of $151 \text{ m}^2 \text{ s}^{-2}$ and RB98 found a median SRH of $180 \text{ m}^2 \text{ s}^{-2}$. However, D93a found a mean of $304 \text{ m}^2 \text{ s}^{-2}$. This could be due to the fact that the dataset used in D93a consisted mostly of large tornadoes (of the six storms observed, four produced a tornado of F3 or greater). It has been shown that the more intense the tornado, the greater the helicity required to support it (Colquhoun and Riley 1996).

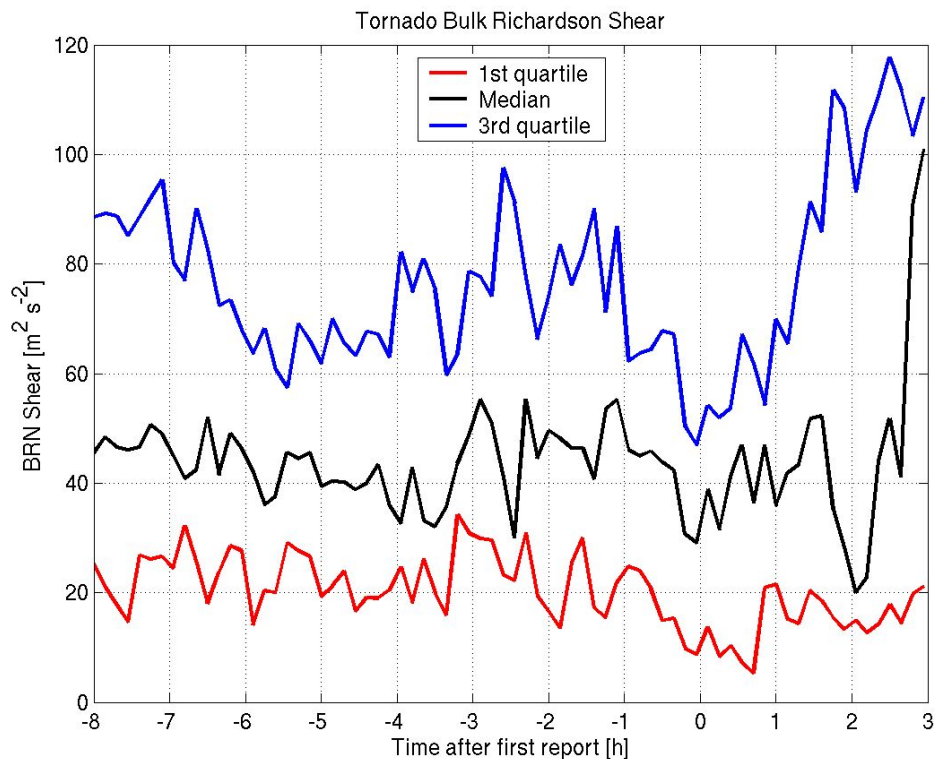


Figure 5.7: As in Figure 5.6, but for Bulk Richardson Shear (BRN shear).

Bulk Richardson Shear (BRN Shear, Figure 5.7) is the denominator of the Bulk Richardson Number (BRN). Since it is a simple measure of shear, it is occasionally used to quantify the magnitude of wind shear present in a given environment although few

benchmark values can be found in the literature. Like helicity, the median value of BRN shear is mostly constant during the pre-storm environment and increases after the tornado forms.

b3. Combined indices

Combined indices use both a measure of buoyant instability and wind shear to quantify the ability of the environment to support rotating updrafts. Both AERI and NPN observations are used for the following figures.

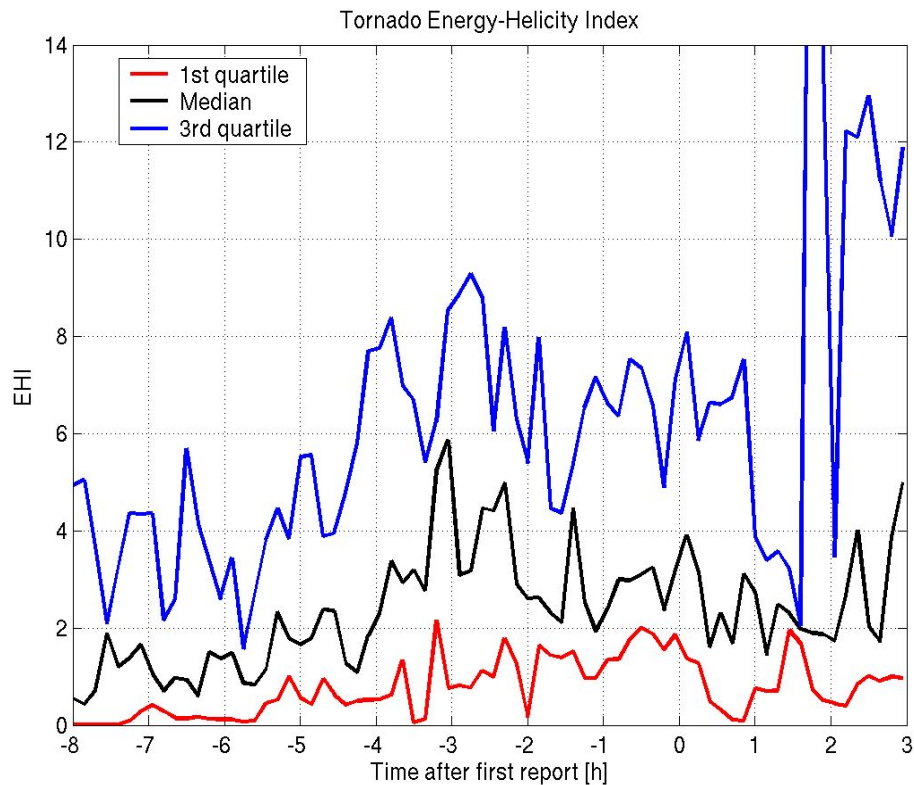


Figure 5.8: Plot of the quartile values of Energy-helicity Index (EHI) for all tornadic events in the SGP domain from eight hours before touchdown to three hours after touchdown as retrieved from AERI and NPN data. The first quartile is denoted in red, the median in black, and the third quartile in blue.

The plot of Energy-helicity Index (EHI, Figure 5.8) shows an increase until a short time before tornado formation, and then decreasing values after that. This is expected since EHI is proportional to the product of CAPE and SRH. If CAPE exhibits a trend where it peaks an hour before tornadogenesis while SRH remains fairly constant, then the EHI trend will roughly mirror that of CAPE. The values of EHI in this study are within the range found in past studies: RB98 measured a mean EHI of 1.48 for tornadic storms, while the mean values for D93a and D93b are 3.6 and 2.5 respectively. Due to the reliance of EHI on helicity in D93a it is reasonable to expect that D93a would find larger values of EHI than other studies.

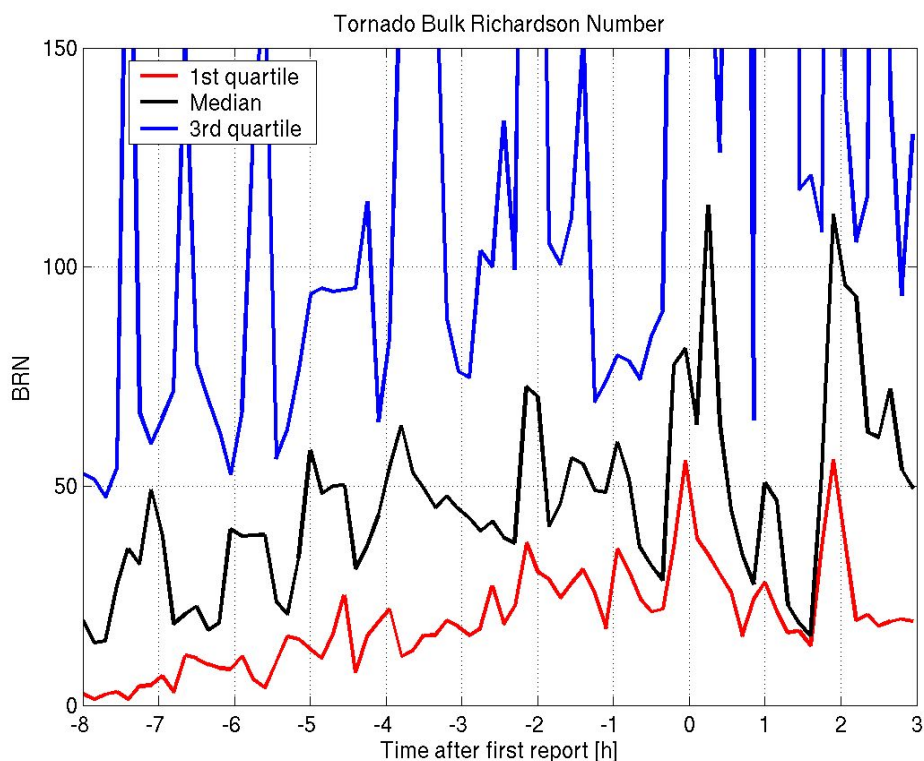


Figure 5.9: As in Figure 5.8, but for Bulk Richardson Number (BRN).

The plot of Bulk Richardson Number (BRN, Figure 5.9) shows a definite increase in value with time until the tornado forms. Prior studies found a large range of typical values for BRN: RB98 found a median value of 7.5, while D93b found a mean value of 42. The median values found several hours before tornado formation in this study correspond well to that range, but those previous studies are unable to capture the clear change in BRN as time progresses. Because BRN is a ratio of CAPE to a measure of shear, slight changes in the shear parameter will cause BRN to greatly fluctuate, especially when the shear parameter is small. This behavior is clearly visible in Figure 5.9.

C. Non-tornadic supercell results

To see if these instruments can assist forecasters in the process of discriminating between tornadoes and non-tornadic supercells, the median values for the above indices were plotted for both types of storms. However, these plots are only valid in a qualitative sense. The defining characteristic of a tornadic storm is its tornado, which can clearly be defined as beginning at a specific point in time and space. Unfortunately, the definition for supercell used by this study does not accurately capture the time or location at which updraft rotation begins, and there is no way to judge the time when a potentially tornadic supercell becomes irrevocably non-tornadic. The zero hour on the following plots for non-tornadic storms only represents the earliest time that large hail was reported; the moment of supercell development could come substantially earlier than that. Therefore, the plots of median values for both storm types can only be compared for their general trends, rather than specific values at specific times.

c1. Thermodynamic indices

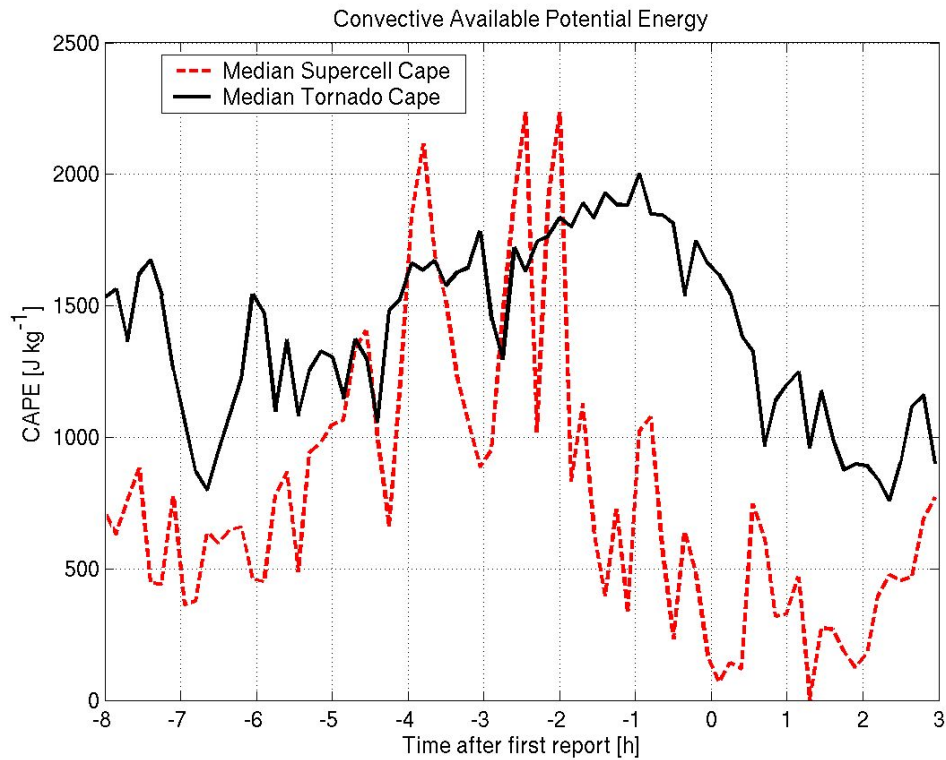


Figure 5.10: Plot of the median values of CAPE for all tornadoes (black) and all non-tornadic supercells (red) in the SGP domain from eight hours before the event until three hours after. The zero hour corresponds with touchdown for tornado cases, or hail report time for the non-tornadic supercell cases.

CAPE for non-tornadic supercells is generally lower than it is for tornadic storms, especially as the time of tornado formation approaches (Figure 5.10). CAPE for the non-tornadic cases peaks two hours before a similar peak occurs in the tornadic cases, with environmental instability remarkably low during hail formation. RB98 found that median CAPE for non-tornadic supercells (1152 J kg^{-1}) was similar to tornadic storms (1314 J kg^{-1}).

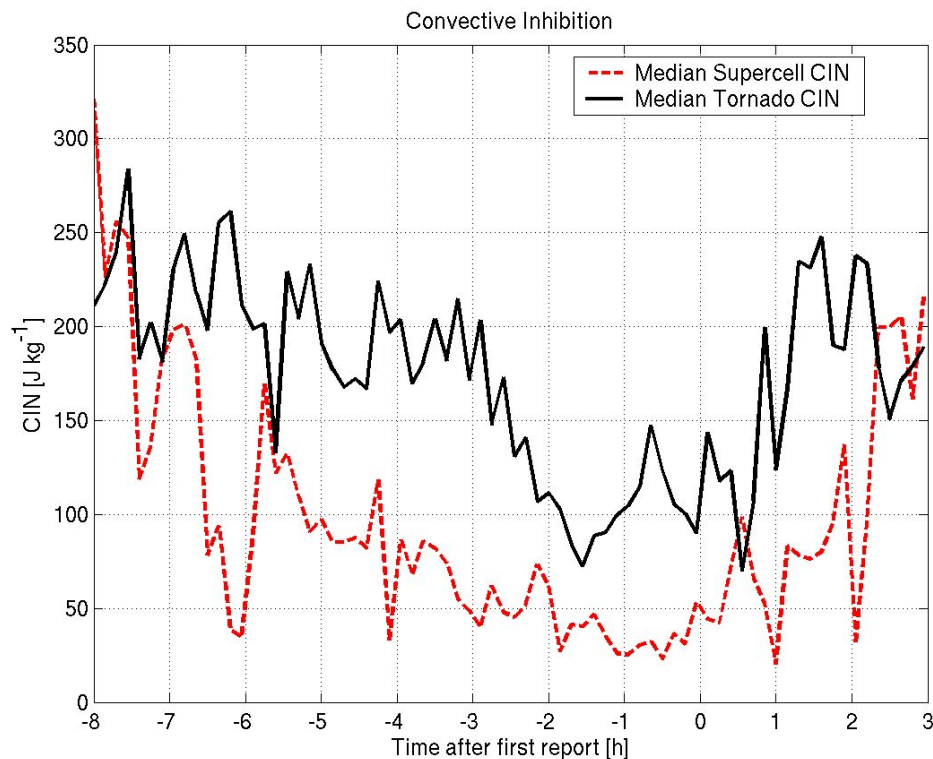


Figure 5.11: As in Figure 5.10, but for CIN.

The median plots of CIN as measured by AERI (Figure 5.11) show that tornadic storms generally have greater CIN than non-tornadic ones. This is contrary to the findings of RB98, which found that CIN in non-tornadic supercells was larger than tornado-producing storms, at 35 J kg^{-1} and 12 J kg^{-1} respectively. Like the tornadic storms, non-tornadic CIN decreases as the time of storm formation approaches and increases after the event. It is interesting to note that the extreme ends of the time range analyzed have similar CIN despite hosting different types of storms.

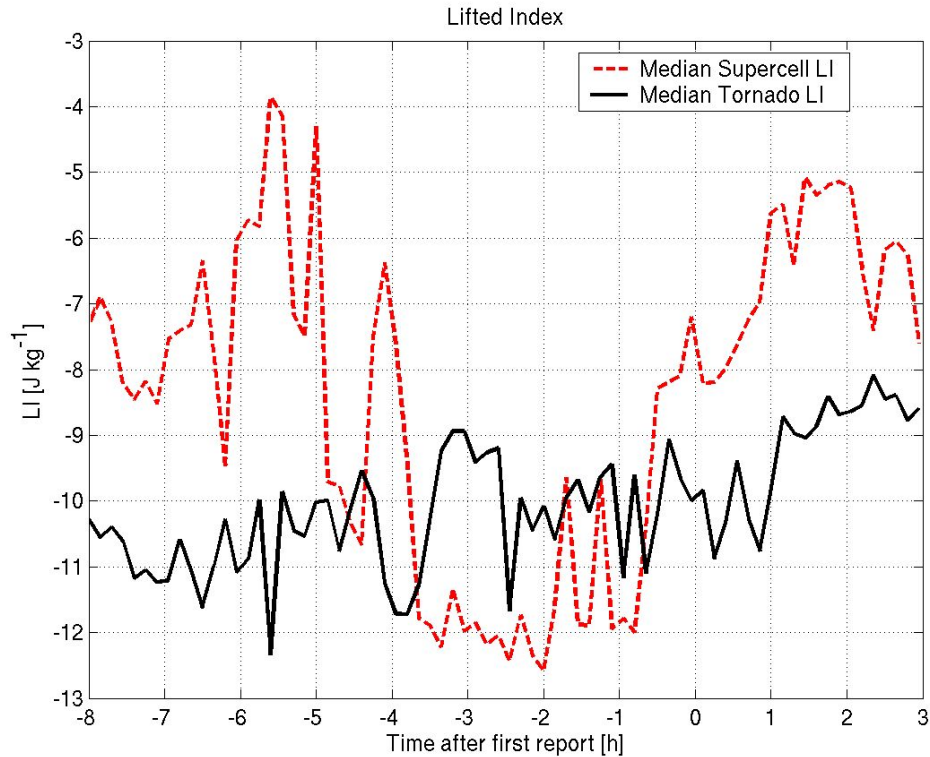


Figure 5.12: As in Figure 5.10, but for LI.

The median plot of non-tornadic supercells (Figure 5.12) shows a marked increase in instability between four and five hours before the large hail report, followed by a decrease starting between one and two hours before the large hail report. Like CAPE, the LI indicates that instability for non-tornadic storms is generally less than that of tornadic storms. The greater instability during the time in convection is beginning could be due to the definition of non-tornadic supercell; storms that will support hail of two inches or greater in diameter form in a very unstable environment.

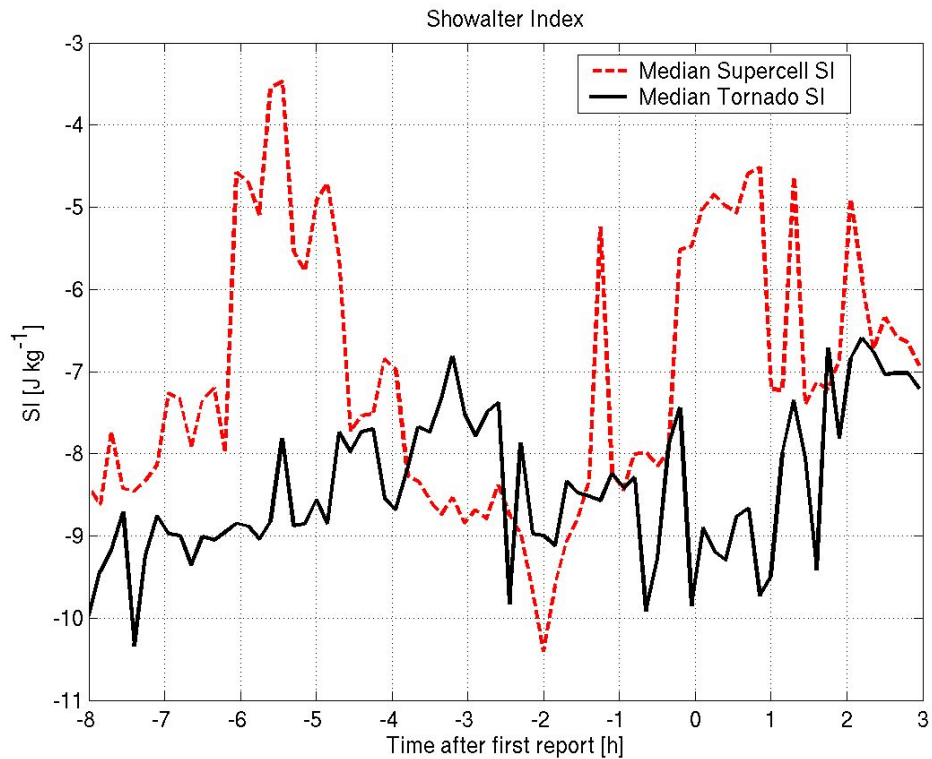


Figure 5.13: As in Figure 5.10, but for LI.

The trend for the median value of non-tornadic supercell SI (Figure 5.13), as expected, shows a general similarity to the median value of non-tornadic supercell LI. Environmental instability is lowest between four and six hours before large hail is reported, and it is greatest at two hours before that time. Instability decreases in the post-hail environment.

c2. Shear indices

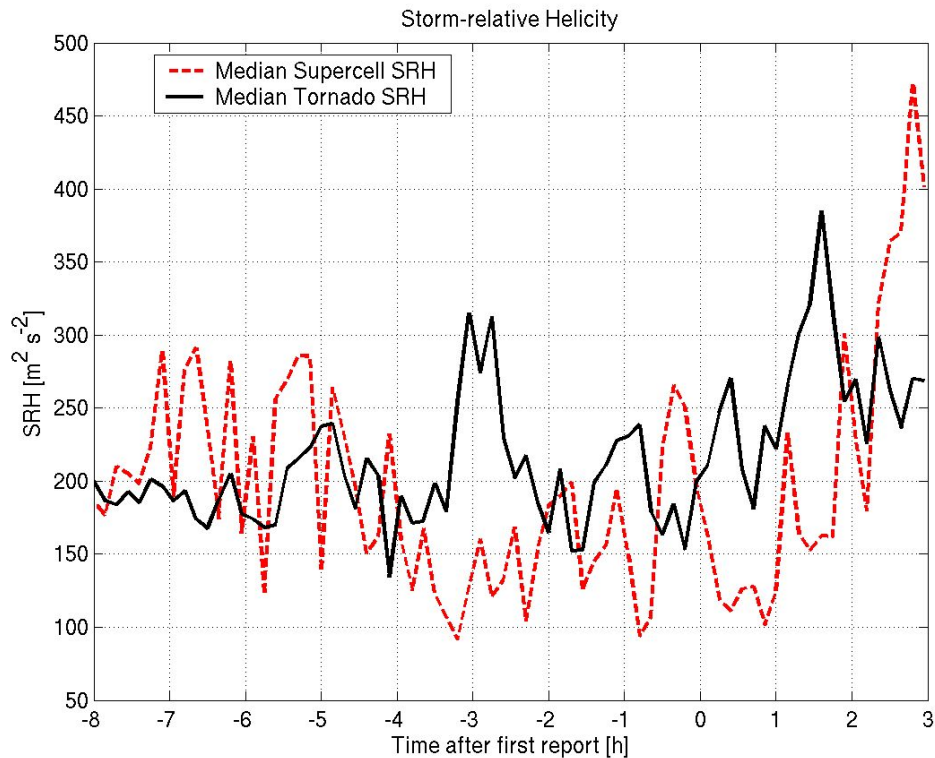


Figure 5.14: As in Figure 5.10, but for SRH.

Whereas tornadic storms show elevated levels of SRH between two and four hours prior to tornadogenesis, non-tornadic storms show lower levels of SRH for that time range (Figure 5.14). The values of SRH for the remainder of the pre-storm environment are very similar which implies the difficulty associated with solely using SRH as a discriminator between tornadic and non-tornadic storms. The NPN-measured range for non-tornadic supercells is similar to other values in the literature: RB98 found a median value of SRH of $124 \text{ m}^2 \text{ s}^{-2}$ while D93a found a mean SRH of $160 \text{ m}^2 \text{ s}^{-2}$.

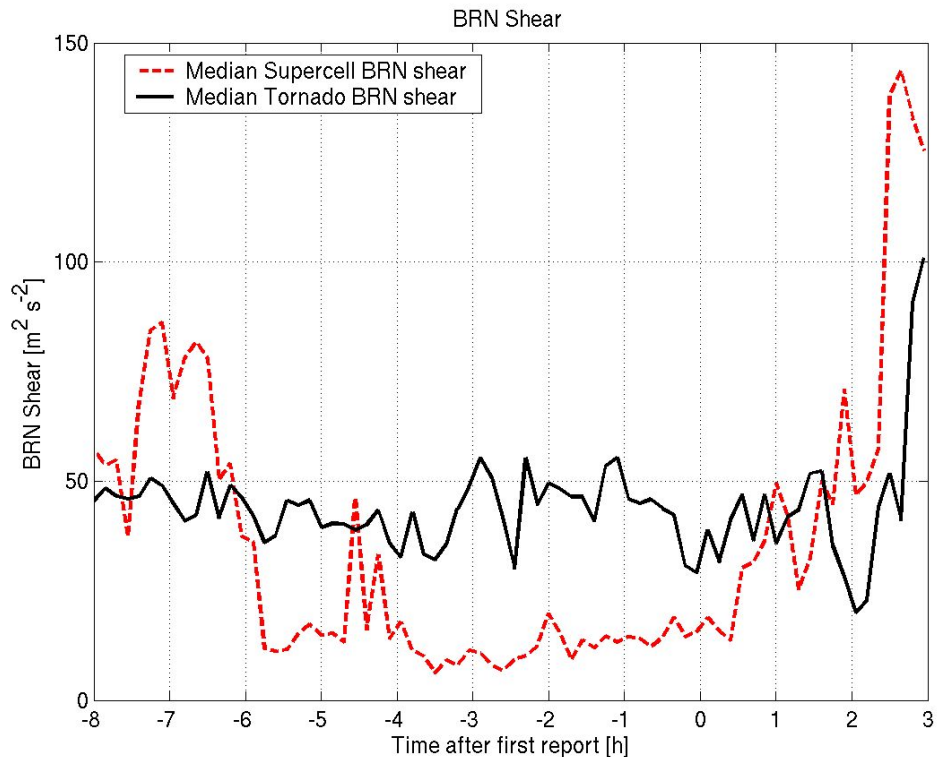


Figure 5.15: As in Figure 5.10, but for BRN Shear.

BRN Shear (Figure 5.15) is decidedly lower for non-tornadic storms than tornadic ones during much of the pre-storm time. While tornadic BRN shear tends to remain in the range of 40 to 50 $\text{m}^2 \text{s}^{-2}$ in the eight hours before tornadogenesis, pre-non-tornadic BRN shear from six hours before reported hail until one-half hour following the initial hail is substantially lower at 10 to 20 $\text{m}^2 \text{s}^{-2}$.

c3. Combined indices

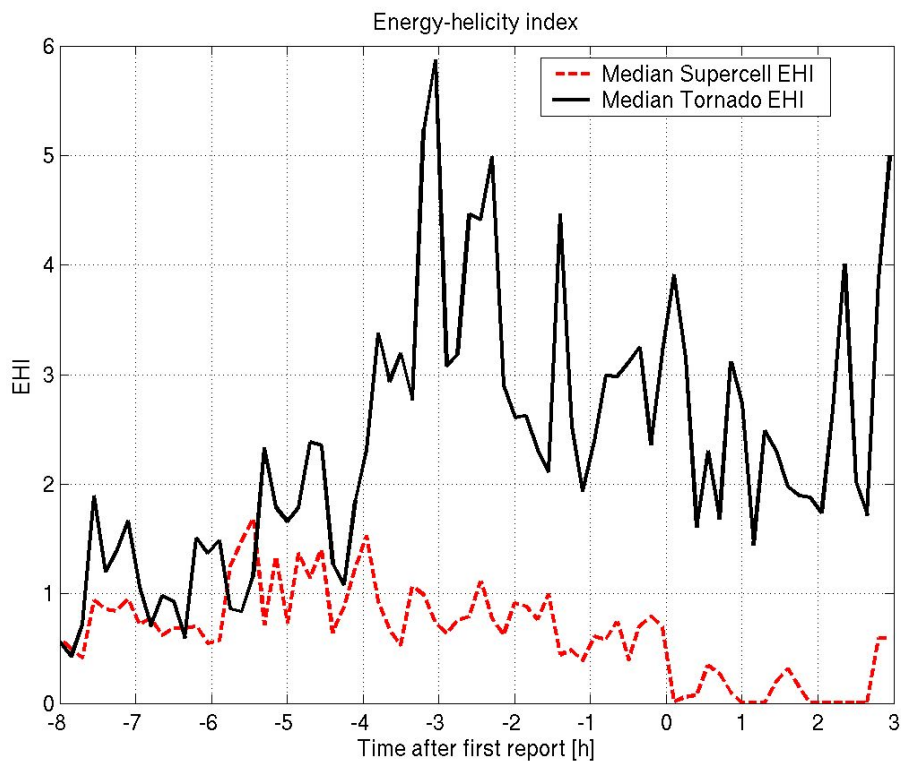


Figure 5.16: As in Figure 5.10, but for EHI.

EHI (Figure 5.16) shows promise as a discriminator between tornadoes and non-tornadic storms. While EHI values for tornadic and non-tornadic storms are similar from four to eight hours before the severe weather report, after that time the tornadic EHI increases greatly. However, the non-tornadic EHI shows a slight decreasing trend during that time. Operationally, if EHI values continued to rise as the day progressed, forecasters could continue to monitor the situation for tornado development. If EHI values remained constant, however, the primary threat would likely be large hail. These possibilities will be further

examined in the case studies in the following chapter. The median value for non-tornadic supercells in RB98 was 0.64 while it was 1.2 in D93a.

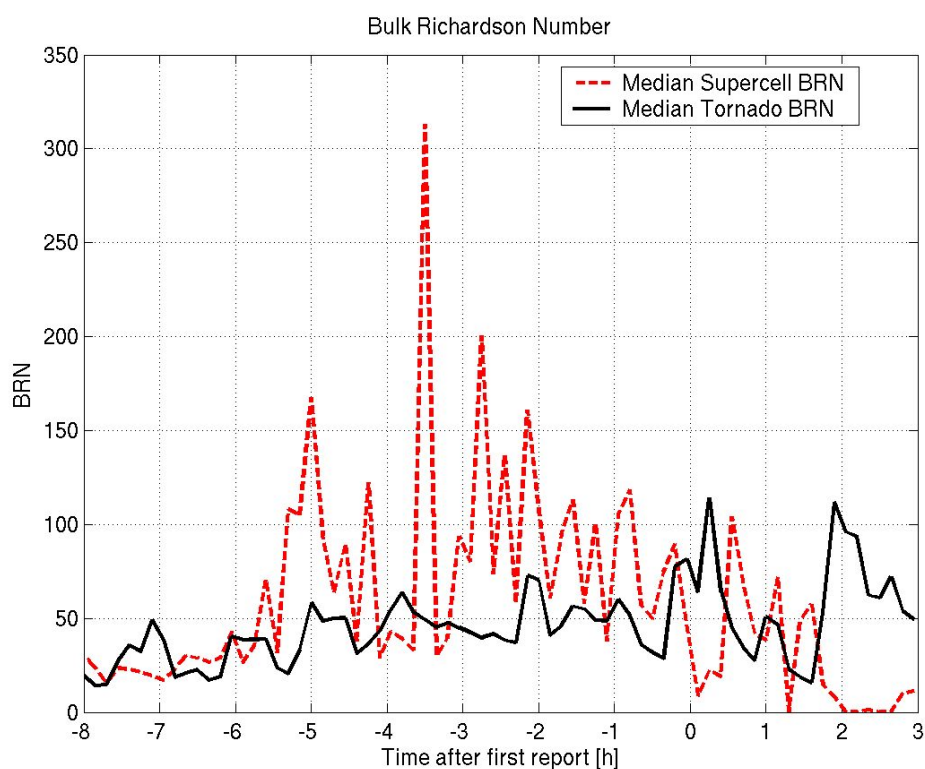


Figure 5.17: As in Figure 5.10, but for BRN.

Generally, the median value of BRN (Figure 5.10) for non-tornadic supercells was higher than that of tornadic ones. The low-shear environment of the non-tornadic storms is evident in the plot of BRN: since the shear is so small and since it is in the denominator of the BRN formula, slight changes in shear will result in large changes for BRN. RB98 found that BRN is not a good discriminator between non-tornadic and tornadic supercells, with median values of 6.6 and 7.5 respectively.

D. Changes

With many observations per storm, the combined AERI and NPN measurements not only allow the opportunity to investigate the evolution of stability before severe weather events, they also can be used to look at rates of change of those indices.

One such measure of a rate of change for six of the indices discussed herein is defined by the following formula:

$$I(t) = \frac{I_t - \bar{I}}{\bar{I}}$$

where I_t is the value of an index at time t , and \bar{I} is the mean value of that index for the previous hour. This parameter captures perturbation from a running mean normalized to the running mean. The median values of this parameter for both tornadic storms and non-tornadic supercells are plotted in Figure 5.18. As expected, these are noisy time series, as this parameter is similar to a derivative and higher order operations are noisier than lower-order ones.

Still, there are some trends evident in these plots. A downward trend in stability change (from larger positive change, to no change, to larger negative change) is evident for both tornadoes and non-tornadic supercells in CAPE and LI. The combination thermodynamic/kinematic both show rapid change following hail formation in non-tornadic supercells.

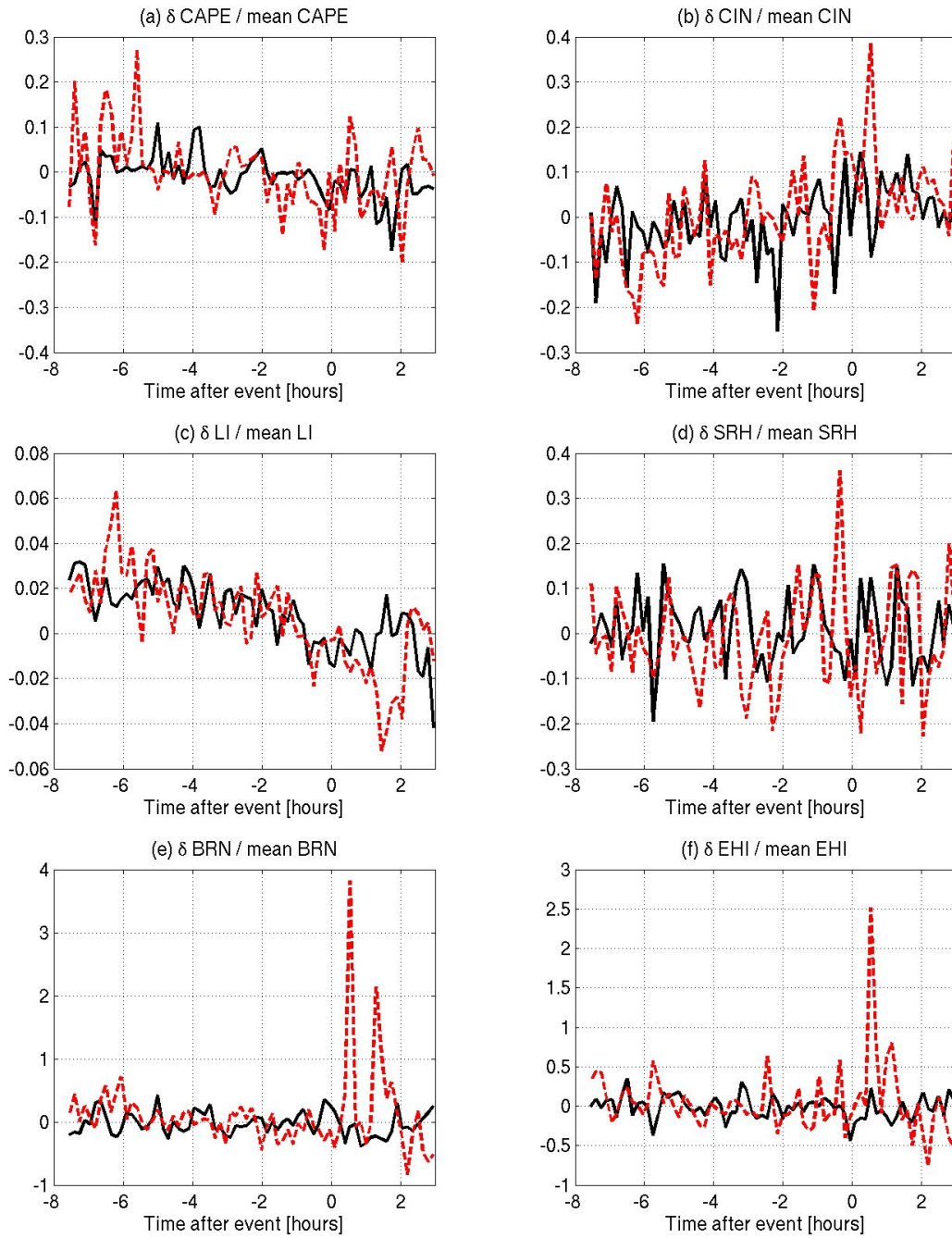


Figure 5.18: Plots of a unitless change parameter for tornadoes (black) and supercells (dashed red) for six indices from 8 hours before event formation to three hours after. The indices shown are (a) CAPE, (b) CIN, (c) LI, (d) SRH, (e) BRN, and (f) EHI.

This section has presented median values for many of the most commonly used severe weather forecast indices. There is significant variability from storm to storm and case to case. This will be explored in the next chapter as two substantially different cases are studied using AERI and NPN observations. While this chapter investigated the application of remote-sensing technology to determine general benchmark values, the next will use these individual case studies to further portray the usefulness of these instruments for nowcasting purposes.

VI. Case studies

Should a combined network of AERI and NPN become operational, one of its most important potential contributions is in nowcasting and operational forecasting (Feltz and Mecikalski 2002). These observations can be used to augment numerical weather prediction models, which can suffer from decreased accuracy in precipitation forecasts up to three hours after initialization time due to model spin-up (Golding 2003). Two case studies are presented below to demonstrate the usefulness of these instruments for these purposes.

A. 8-9 May 2003

May 2003 was an extremely prolific month for tornado formation. During this month 543 tornadoes formed, more than any other calendar month (Hamill et al. 2005). This included the week of 4-10 May 2003, which had the record number of reported tornadoes of any week. Of particular interest were the tornadoes of 8-9 May 2003, when seven tornadoes formed within the experiment domain. A map of these tornadoes can be seen in Figure 6.1

Surface conditions during that time were warm and humid, aided by surface flow from the southeast that advected moisture from the Gulf of Mexico. A low level jet from the southwest was present at 850 hPa, and a 500 hPa jet came from the west. Together, these wind flows created a profile with a significant amount of shear over Oklahoma and Kansas. Coupled with the instability associated with the strong moisture advection, the environment was ripe for the production of supercells. A composite chart produced by the Storm Prediction Center of the synoptic conditions is shown in Figure 6.2.

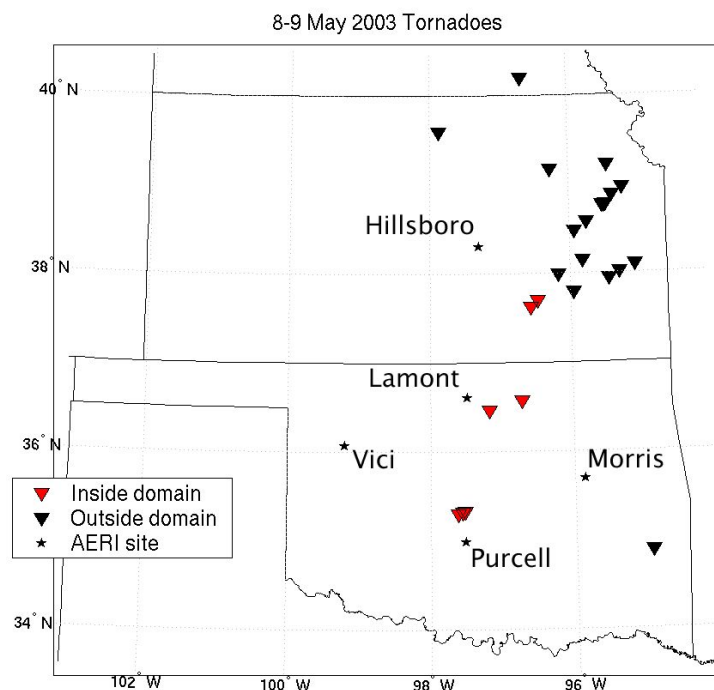


Figure 6.1: Map showing the location of tornadoes during the 8-9 May 2003 tornado outbreak. Red triangles denote the locations of tornadoes within 100 km of an AERI installation, while black triangles denote tornadoes further away than that radius. AERI locations are marked with stars.

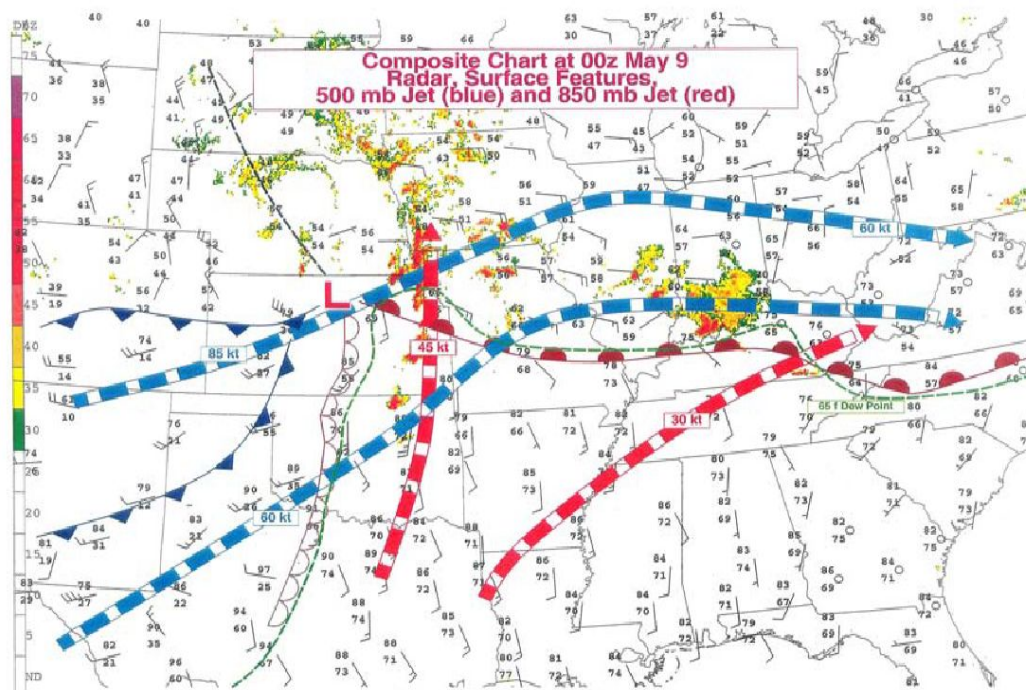


Figure 6.2: Composite chart showing the synoptic conditions at 0000 UTC on 9 May 2003 (7:00 PM CDT, 8 May) over the central United States. The low-level jet is shown in red, the 500 hPa jet is in blue. Fronts and surface conditions are shown using the standard convention. Of particular interest is the dryline, shown here in open, closely-spaced semicircles. From National Weather Service (2004).

Convection initiated around 1730 UTC as the dryline propagated westward. The dryline propagation is clearly evident in time-height cross sections of moisture from AERI (Figure 6.3). Once convection began, the highly unstable air and the strong shear of the wind combined to form supercellular storms. Satellite images of the evolution of these storms are given in Figure 6.4. The first tornado inside the experiment domain formed at 2200 UTC (5:00 PM CDT) outside Moore, Oklahoma, 36 kilometers north-northwest of the AERI/NPN installation at Purcell. This tornado grew to be the most intense of all the tornadoes on that day, registering a level of F4 on the Fujita scale, injuring 139 people, and causing damage of \$370 million (National Climatic Data Center 2003b).

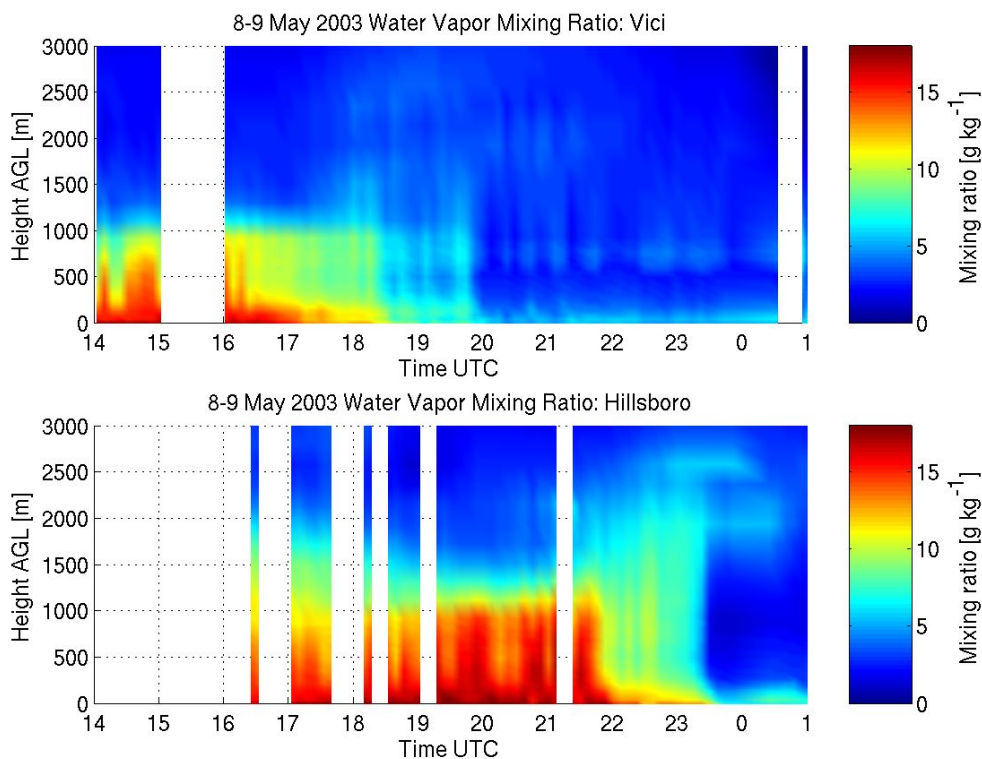


Figure 6.3: A time-height plot of water vapor mixing ratio at Vici, Oklahoma, (top) and Hillsboro, Kansas (bottom) from 1400 UTC on 8 May to 100 UTC on 9 May 2003. The passage of the dryline is clearly evident in the large decrease in mixing ratio with time. Vici is southwest of Hillsboro, so the dryline passage is earlier. The moist layer depth is shallower at Vici than at Hillsboro due to elevation differences: Hillsboro is at an elevation of 446.5 meters above sea level while Vici is at 647.7 meters above sea level.

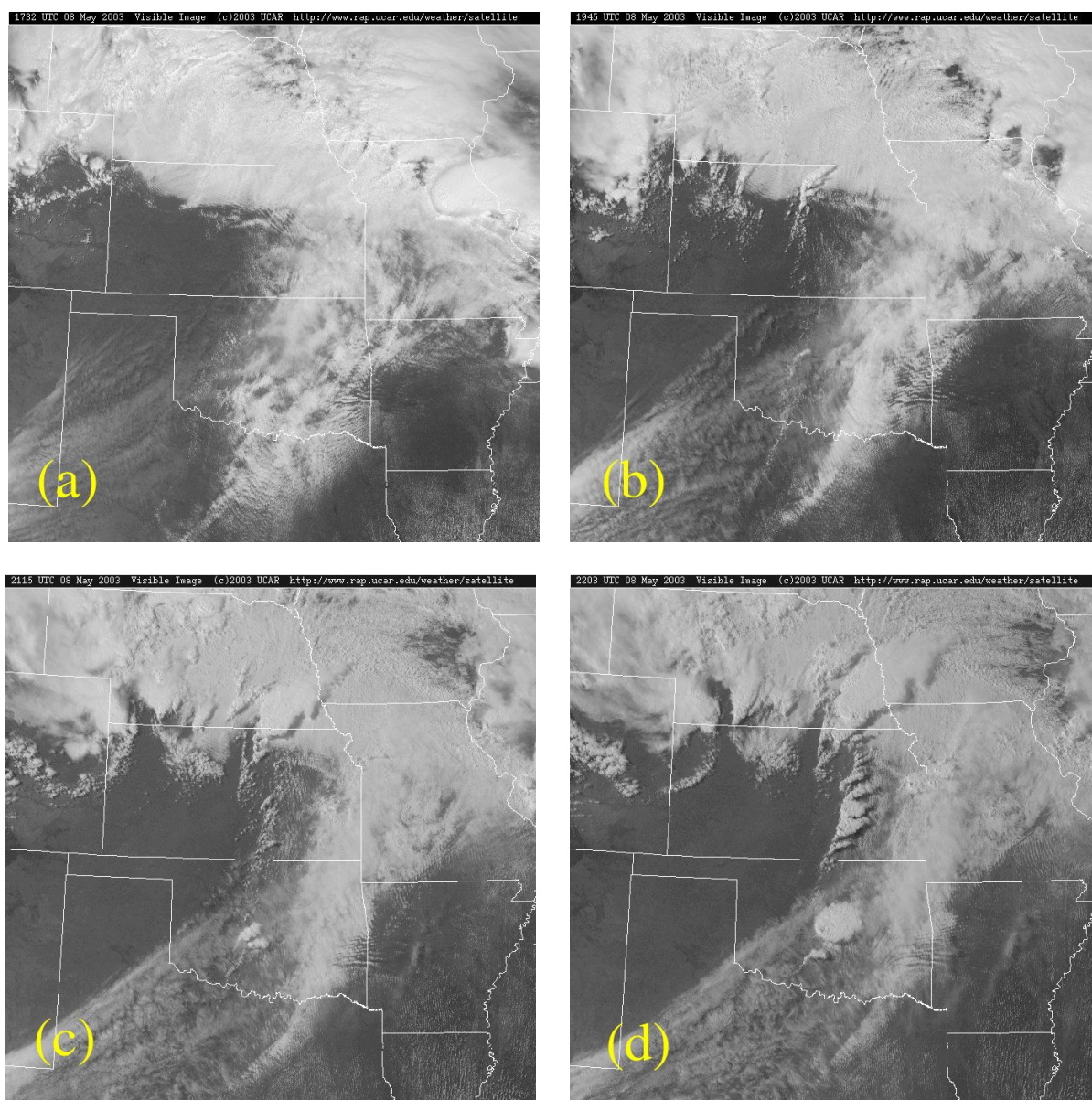


Figure 6.4: Visible geostationary satellite images centered over Wichita, Kansas, showing the evolution of the 8-9 May 2003 tornadic storms. (a) 1732 UTC (12:32 PM CDT), showing the first evidence of convection in western Oklahoma with the passage of the dryline. (b) 1945 UTC (2:45 PM CDT), showing convection along the length of the dryline down into Texas. (c) 2115 UTC (4:15 PM CDT), showing the towering cumulus that eventually developed into supercells. (d) 2203 UTC (5:03 PM CDT), a few minutes after the touchdown of the first tornado in the AERI domain. The tornadic storm is clearly evident in the center of the state of Oklahoma. Satellite images from National Center for Atmospheric Research (NCAR) Mesoscale and Microscale Meteorology Division (MMM),

Due to clouds over the eastern and southern portion of the experiment domain throughout the day, few AERI retrievals are available for times during the development of this storm system. Retrieval availability from the other three locations is much greater. The following figures show convective indices calculated from AERI and NPN profiles. The vertical dashed lines in these plots correspond with the times of the satellite images in Figure 6.4.

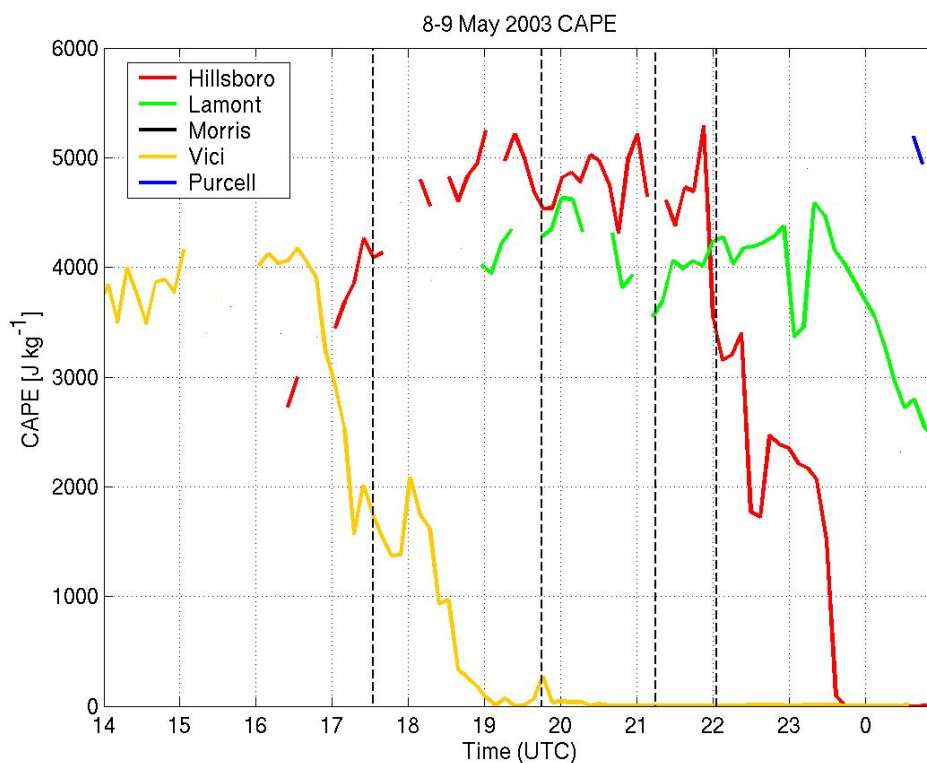


Figure 6.5: Plot of AERI-retrieved CAPE from 1400 UTC on 8 May 2003 through 100 UTC on 9 May 2003 for all AERI sites in the Southern Great Plains. The vertical dashed lines correspond to the times of the satellite images shown in Figure 6.4.

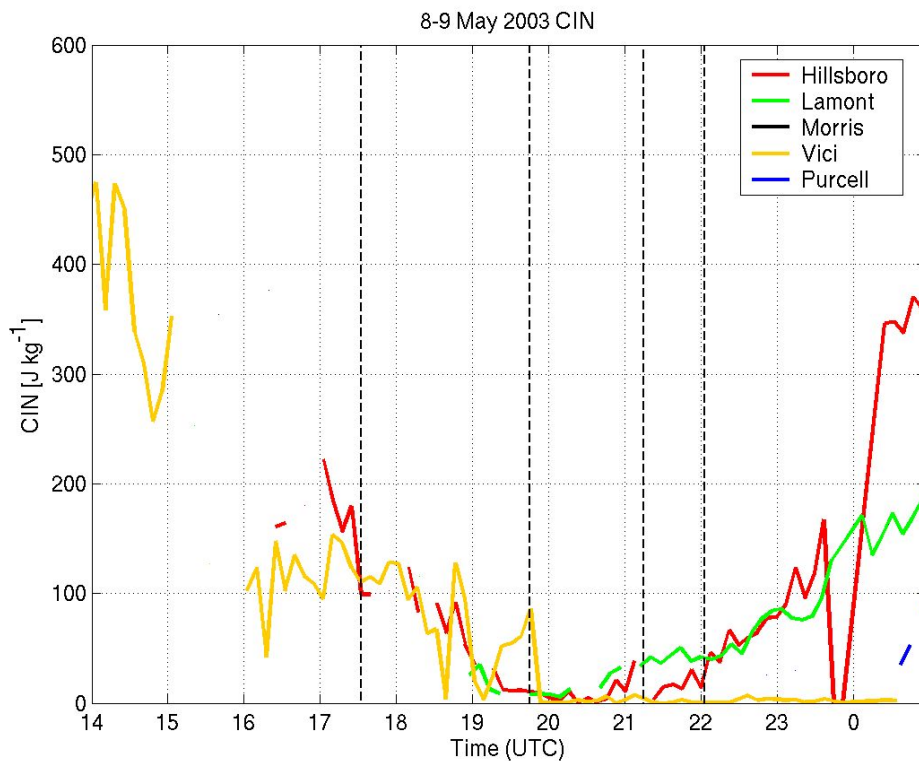


Figure 6.6: As in Figure 6.5, but for CIN.

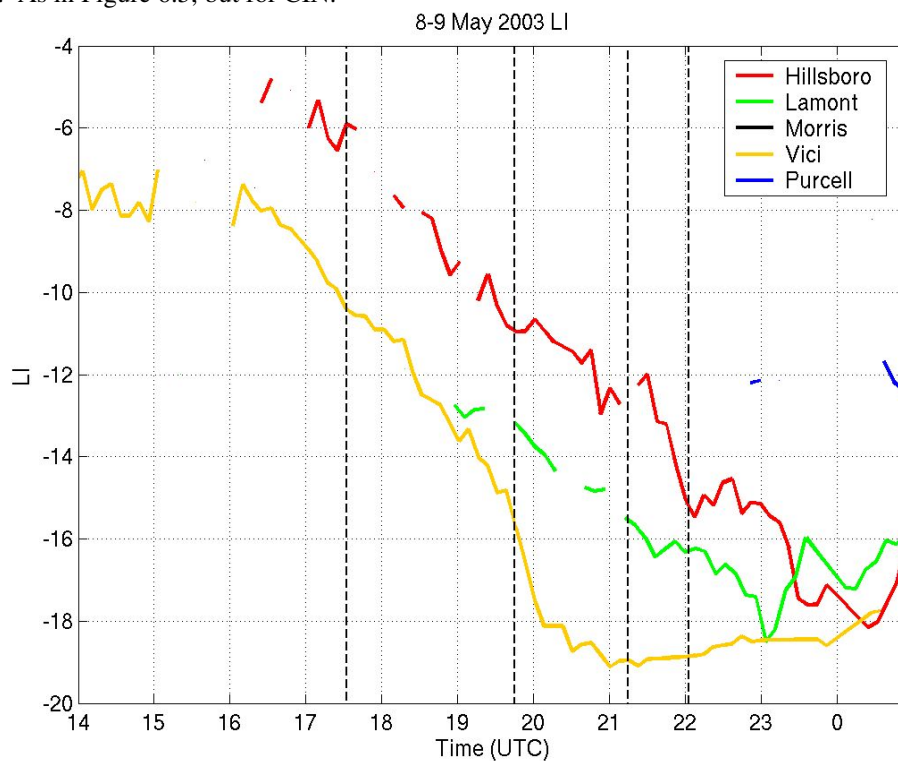


Figure 6.7: As in Figure 6.5, but for LI.

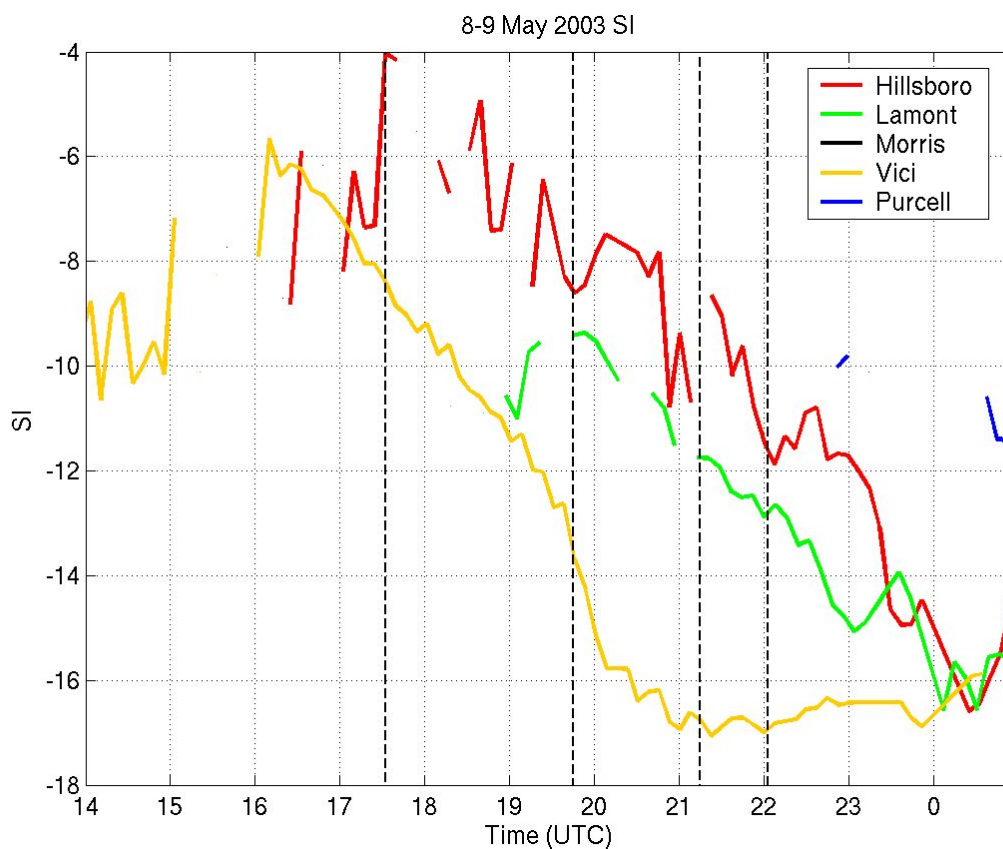


Figure 6.8: As in Figure 6.5, but for SI.

Convection initiated at 1730 UTC as the dryline passed through Vici. The CIN (Figure 6.6) dropped rapidly from 300 J kg^{-1} to 100 J kg^{-1} between 1500 UTC and 1600 UTC, ahead of the approaching dryline. The lifting induced by the propagating dryline was sufficient to overcome the remaining inhibition. As the dryline propagated westward, the CAPE (Figure 6.5) over Vici was depleted, but the LI and SI (Figures 6.7 and 6.8) continued to become more negative, indicating greater instability. A possible explanation for this is the loss of all but surface moisture with the propagation of the dryline. Since CAPE is a layer-integrated quantity while LI and SI are each defined using a single low-level parcel, the depletion of moisture aloft corresponding with the passage of the dryline would cause the

CAPE to vanish. However, the continued presence of moisture right at the surface would result in the creation of a parcel that is assumed to be more unstable than it really is. CAPE is a better measure of atmospheric instability as it accounts for the entire depth of the atmosphere rather than just the lower levels.

Kinematic indices indicated that winds favorable for rotational development were present throughout the SGP domain (Figures 6.9 and 6.10). As the convection propagated eastward, the veering wind combined with the strongest updrafts to create supercells. Eventually, these storms formed very destructive tornadoes.

The combined indices of EHI and BRN (Figures 6.11 and 6.12) show the best analysis of conditions favorable for the support of rotating storms as they take into account both thermodynamic and kinematic instability. The EHI values for several hours before tornadogenesis at Vici are well above the median for tornadic storms. However, as the dryline moved through the area, the CAPE decreased to zero and tornadoes did not form in the vicinity of Vici. Since EHI and BRN are CAPE-dependent parameters, the loss of CAPE is reflected in the time-series for those parameters.

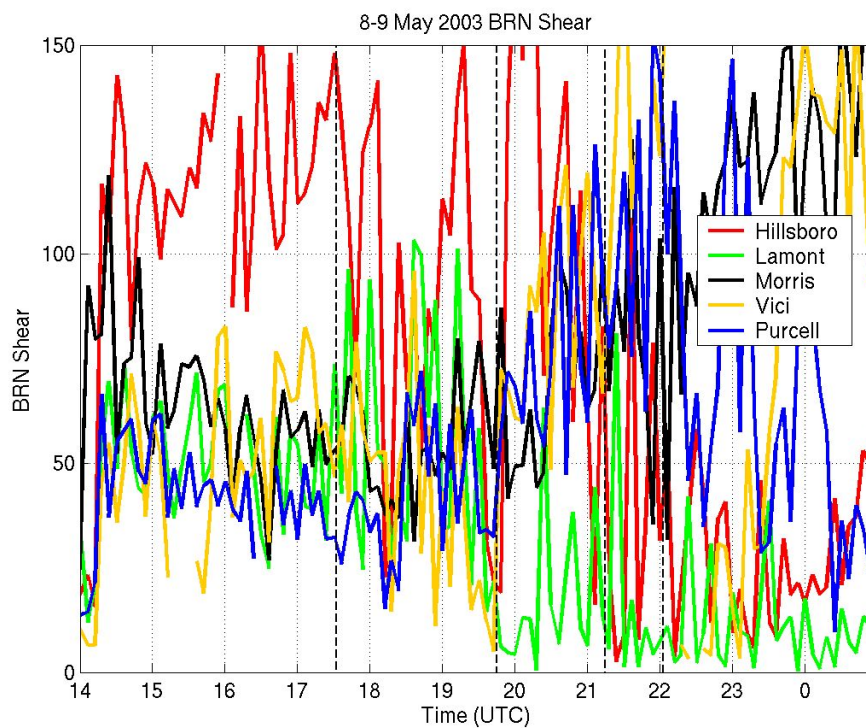


Figure 6.9: As in Figure 6.5, but for SRH as measured by wind profiler.

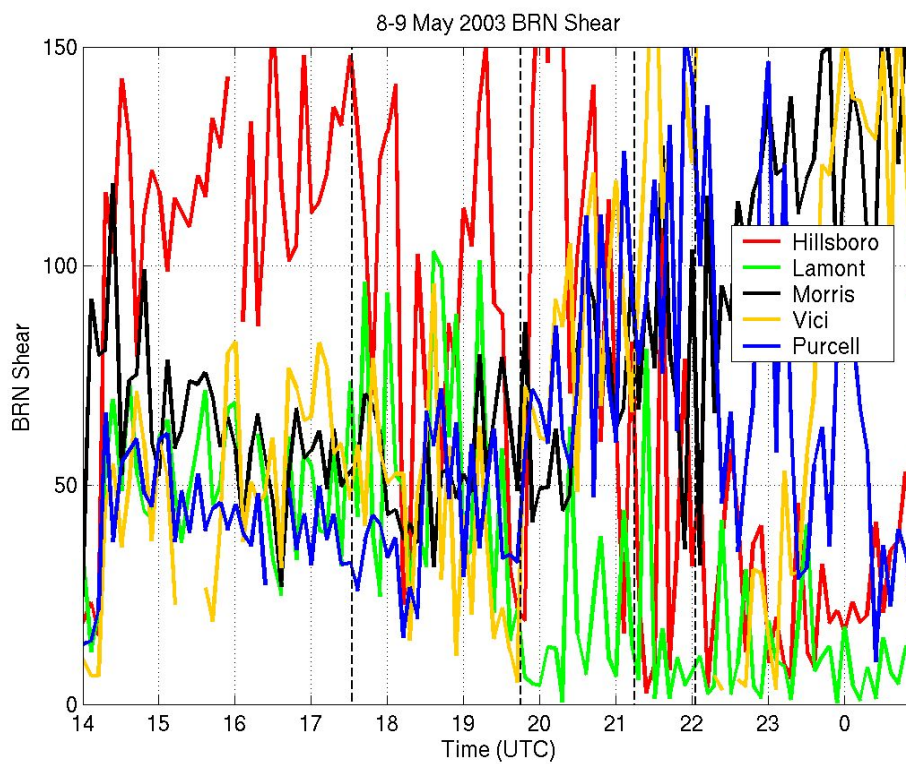


Figure 6.10: As in Figure 6.5, but for BRN Shear as measured by wind profiler.

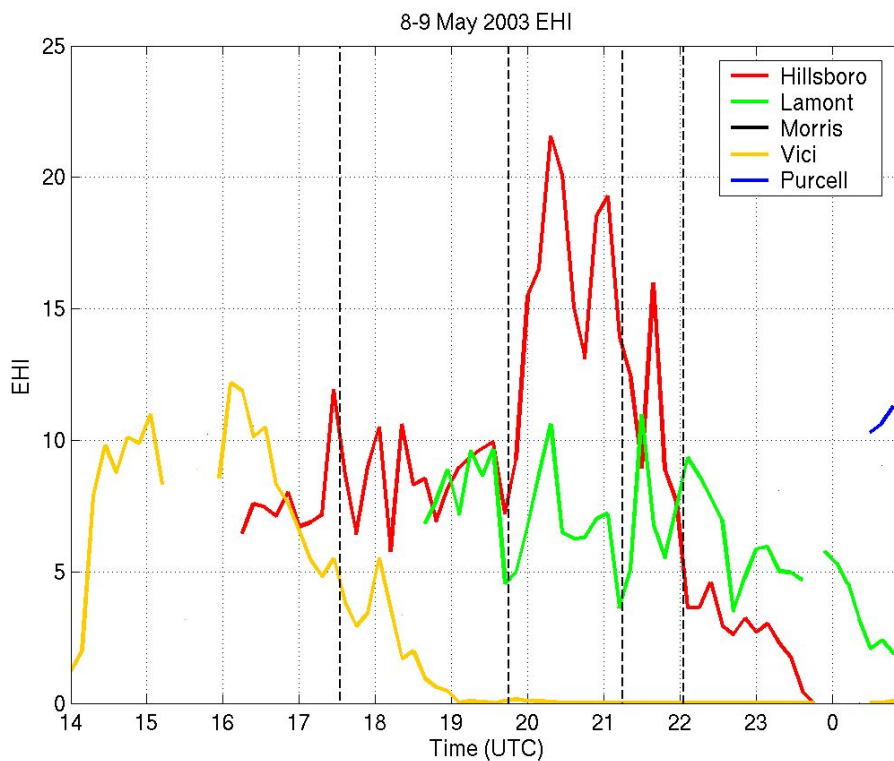


Figure 6.11: As in Figure 6.5, but for EHI as measured by combined AERI and wind profiler observations.

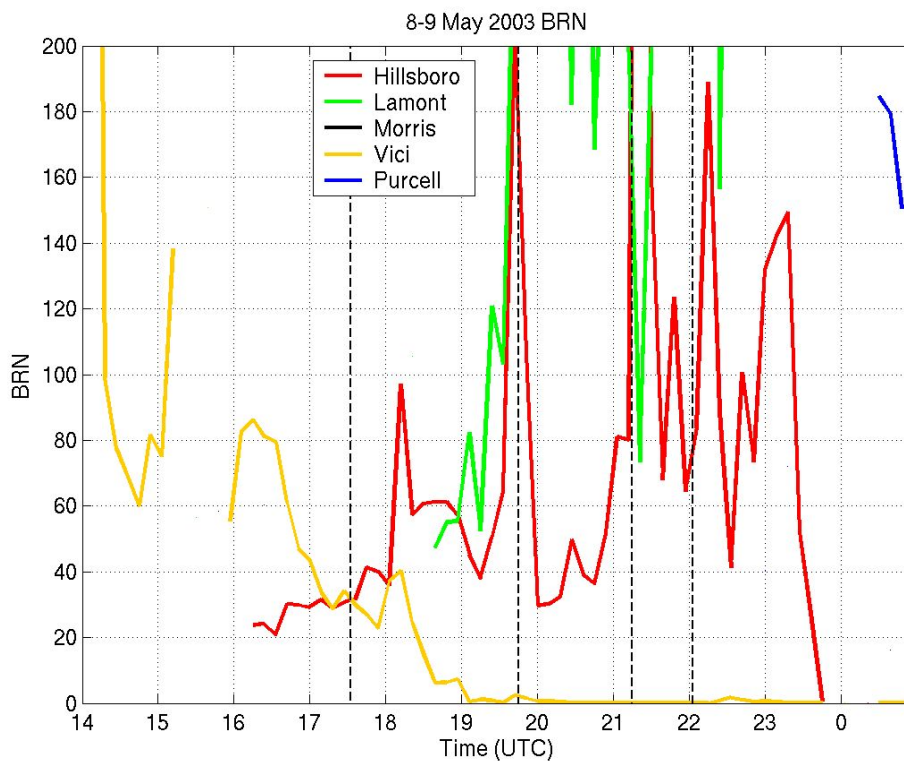


Figure 6.12: As in Figure 6.5, but for BRN as measured by combined AERI and wind profiler observations.

While tornadoes did not form over Vici, the convection that initiated over Vici eventually grew into tornado-producing storms. Even though tornadoes touched down more than 150 kilometers away from Vici, it was the combined influence of the thermodynamic and kinematic characteristics of the atmosphere above western Oklahoma and the Texas panhandle that facilitated the development of nascent cumulus clouds into rotating cumulonimbus clouds. Had the cap not been weakened ahead of the propagating dryline, the storms never would have initiated. If the shear were too weak, the cumulus field would have grown until the initiation of precipitation, at which time evaporative cooling and rainfall would have choked the updraft of these clouds and hindered further vertical development. On the other hand, if the shear were too strong, vertical development would have been stopped by the inability of the atmosphere to support a cohesive vertical updraft.

AERI and NPN observations uncover a wealth of information that standard synoptic rawinsondes cannot provide. On this day, an additional balloon was launched at the asynoptic time of 1800 UTC. Even with the extra sonde, there was still a six hour spacing between upper air observations. Rawinsondes were unable to detect the changes in the depth of the moist layer, the rapid decrease in CIN, the loss of CAPE associated with the passage of the dryline, or any of the multitude of other phenomena visible in the preceding figures.

B. 18-19 September 2002

A drastically different case developed in the experiment domain on 18 September 2002. Instead of a widespread outbreak of tornadoes, this day saw the development of many supercell storms but only two weak tornadoes. The first touched down at 2316 UTC (6:16 PM CDT) near Nash, Oklahoma, while the second touched down slightly more than an hour later at 0028 UTC on 19 September (7:28 PM CDT on 18 September) near Blackwell, Oklahoma. These locations relative to the AERI sites are shown in Figure 6.13. Clearly, the Lamont observation site is closest to the two tornado touchdown points.

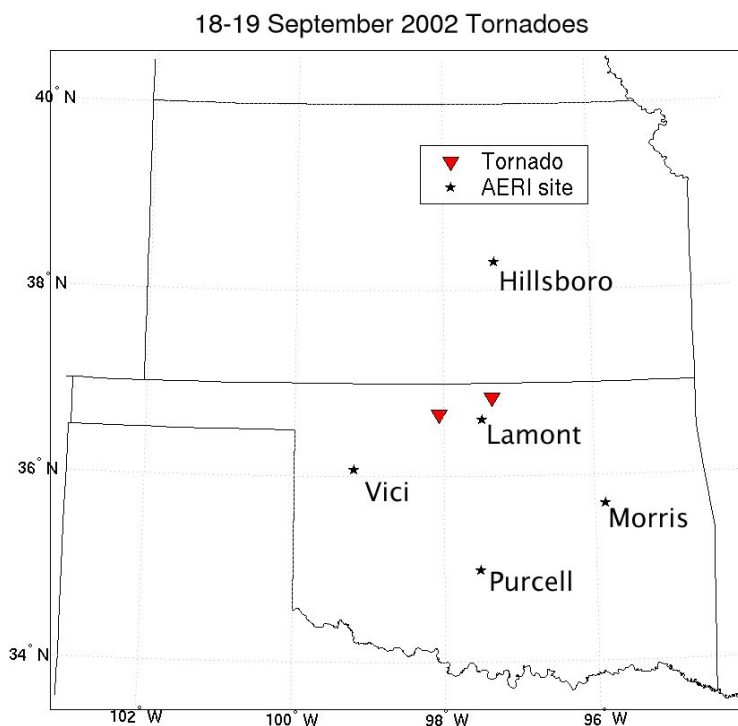


Figure 6.13: Map of the locations of the two tornadoes during the storms of 18-19 September 2002. Tornadoes are marked with red triangles; AERI sites are marked with stars. Both tornadoes that formed during this event were well within the 100 km radius of an AERI site required for it to be considered part of the experiment domain.

Both tornadoes on this day rated at F0 on the Fujita scale. Neither caused any damage or casualties. The first tornado had a path length of 1.6 km and a width of 180 m while the second touched down only very briefly and had a width of 25 m (National Climatic Data Center 2003a).

Significant surface moisture was present across the Southern Great Plains throughout the day, a remnant of earlier moisture advection. An upper-level trough tilted to the west with height created a wind profile conducive to the development of rotating storms. Trailing the surface low associated with the upper-level trough was a cold front, which provided the lifting needed to initiate convection. Surface conditions near the time of convective initiation are displayed in Figure 6.14 while satellite images showing the development of convection can be seen in Figure 6.15

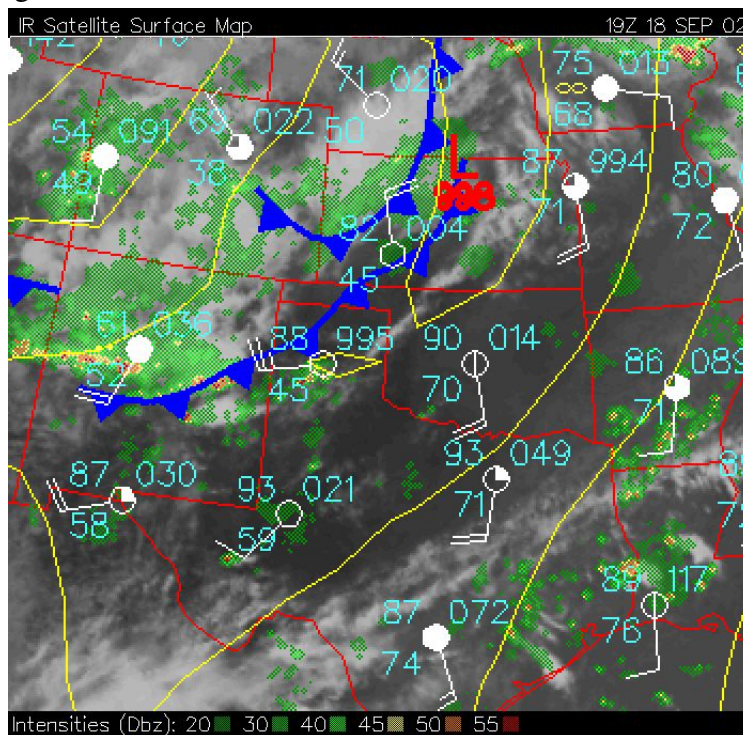


Figure 6.14: Plot of surface conditions in south-central United States at 1900 UTC on 18 September 2002. The cold front is clearly evident stretching along an axis from north-central Kansas to east-central New Mexico. From NCAR MMM.

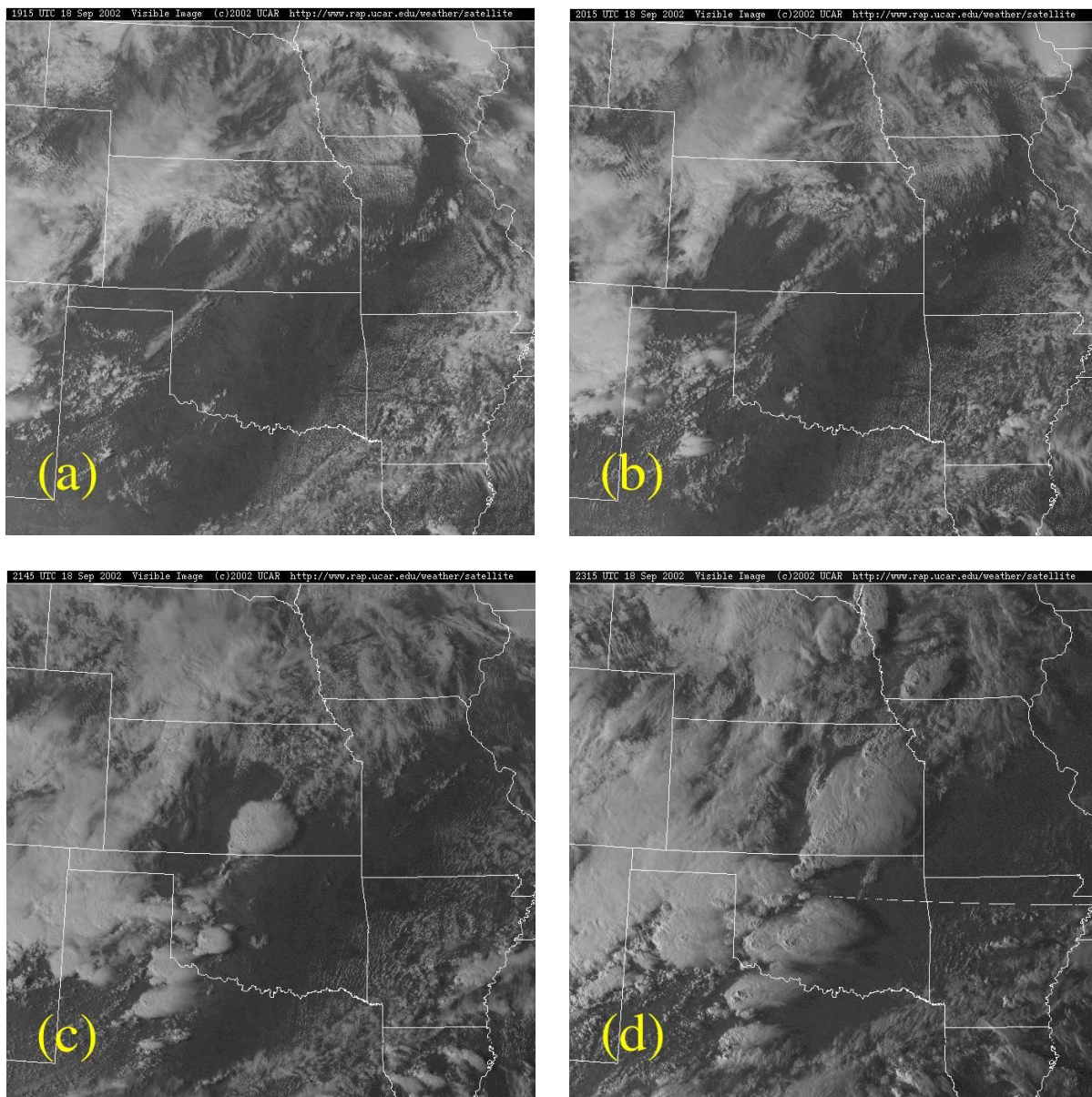


Figure 6.15: Visible geostationary satellite images centered over Wichita, Kansas, showing the evolution of the 18-19 September 2002 tornadic storms. (a) 1915 UTC (2:15 PM CDT), when individual convective clouds are first visible on the satellite image. (b) 2015 UTC (3:15 PM CDT), showing the first towering cumulus (on the Oklahoma/Kansas border) that would later develop into a supercell. (c) 2145 UTC (4:45 PM CDT), showing a line of discrete supercells. (d) 2315 UTC (6:15 PM CDT), one minute before the first tornado touched down. Images from NCAR MMM.

Like the previous case, convection initiated when a passing boundary propagated through a high-instability area where inhibition had been greatly reduced from an earlier peak. The plots of CAPE (Figure 6.16) and CIN (6.17) show this evolution. Prior to the arrival of the cold front, CIN dropped sharply across the entire domain. For example, CIN dropped from 600 J kg^{-1} to less than 150 J kg^{-1} in 90 minutes near Vici, well before convective clouds were visible on the satellite. Once the cold front arrived in the SGP domain, the lifting was enough to overcome the remaining inhibition and reach the level of free convection.

Between 2100 UTC and 2200 UTC, there was a significant drop in CAPE from 3100 J kg^{-1} to 2100 J kg^{-1} at Lamont, the same time that a nearby towering cumulus was growing into a supercell. However, in the thirty minutes prior to tornadogenesis at 2316 UTC, CAPE at Lamont returned to over 3000 J kg^{-1} .

The plots of LI (Figure 6.18) and SI (Figure 6.19) show trends that are very similar to the climatologies of Chapter 5. Instability increases to a maximum at a time between convective initiation and tornadogenesis at which time it decreases. The plot of LI is particularly interesting, as it shows that the locations closest to the line of supercell formation had a larger maximum than the locations farther away from that axis.

All of the thermodynamic indices show a sharp change at Lamont at 0020 UTC due to the arrival of the storm outflow boundary, which caused rapid cooling at the lowest levels and created a strong inversion directly above the site.

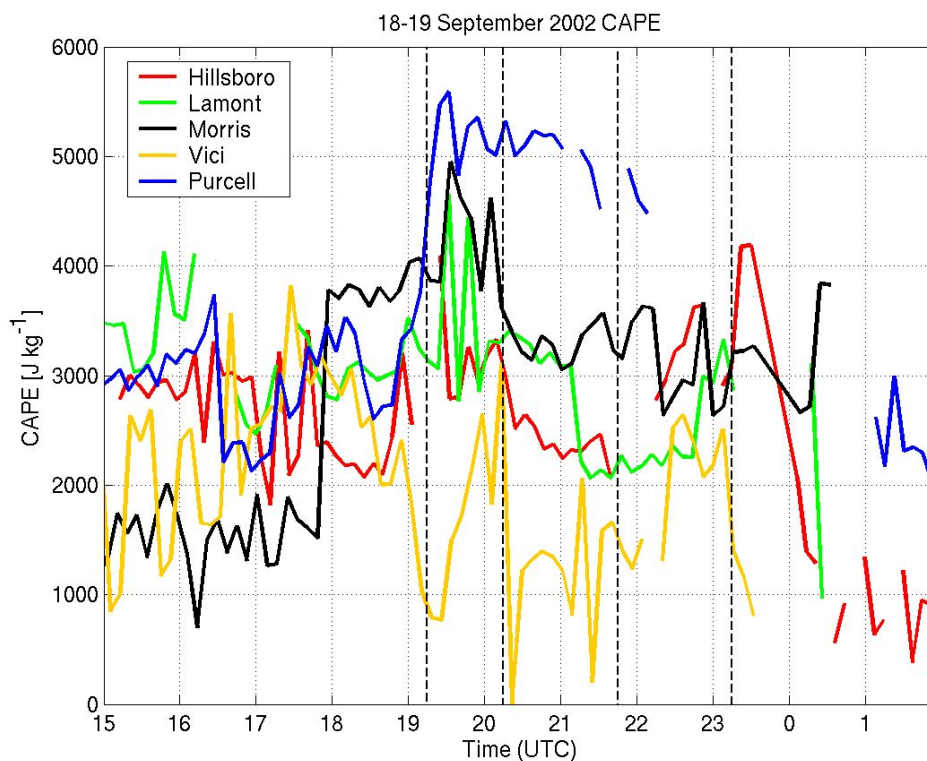


Figure 6.16: Plot of AERI-retrieved CAPE from 1500 UTC on 18 September 2002 through 200 UTC on 19 September 2002 for all AERI sites in the Southern Great Plains. The vertical dashed lines correspond to the times of the satellite images shown in Figure 6.15.

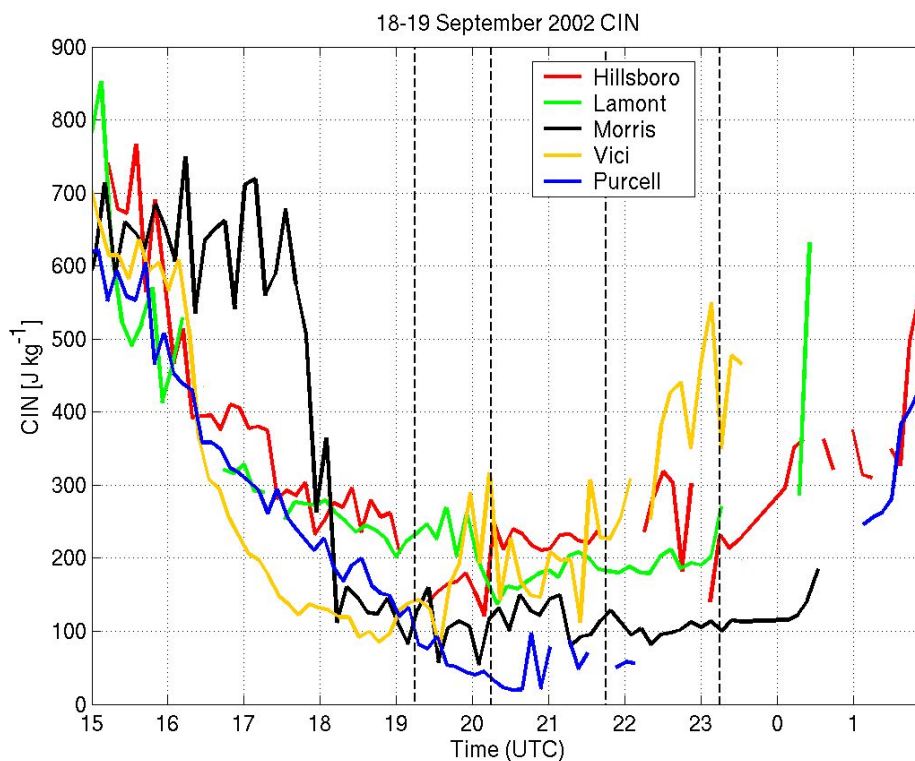


Figure 6.17: As in Figure 6.16, but for CIN.

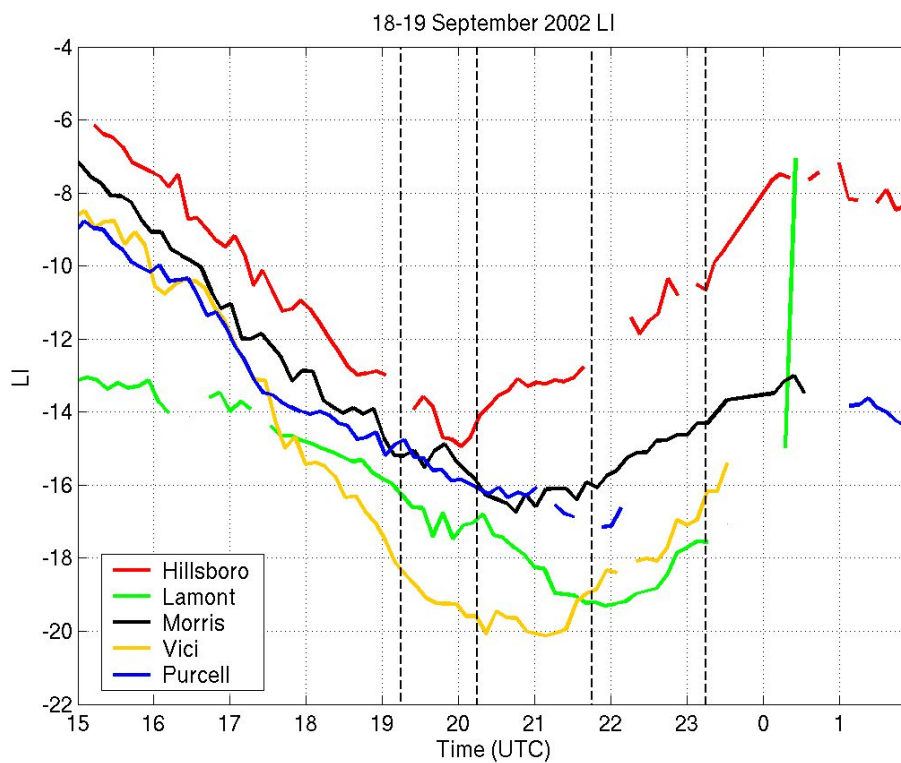


Figure 6:18: As in Figure 6.16, but for LI.

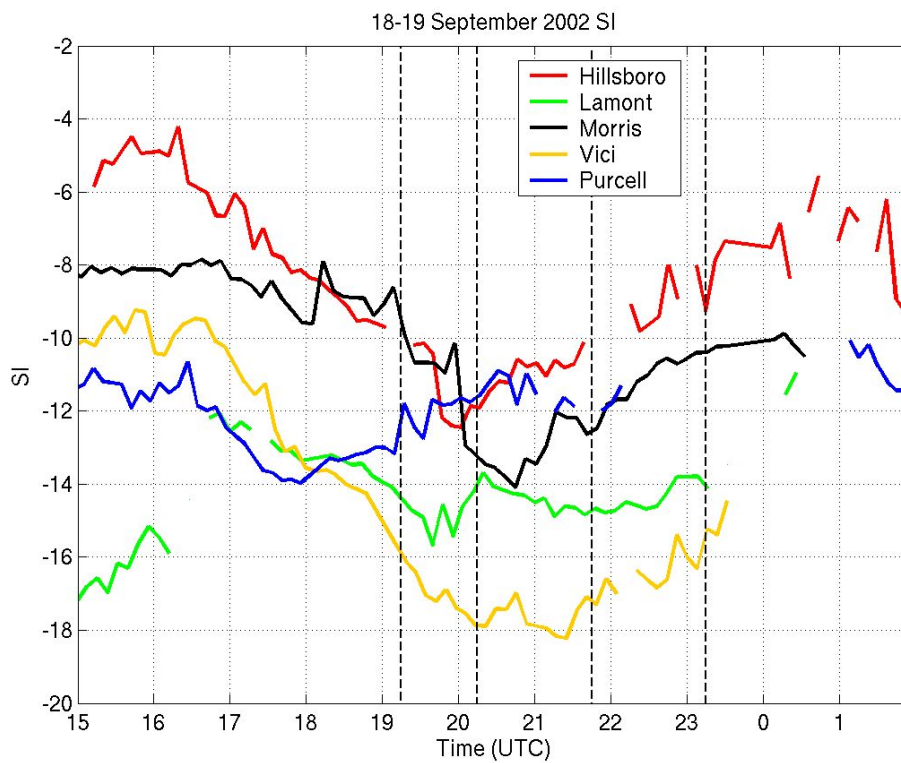


Figure 6:19: As in Figure 6.16, but for SI.

As is typically seen, there is a large degree of variability in the kinematic indices associated with this case. The plots of SRH (Figure 6.20) and BRN shear (Figure 6.21) show that shear overall was less in this case than it was in the 8-9 May 2003 outbreak case but that the remaining stability indices were still significant. Trends are hard to identify in the kinematic indices due to the high variability from observation to observation.

The combined thermodynamic/kinematic indices of EHI (Figure 6.22) and BRN (6.23) show that this case has indices typically associated with tornadic supercells. The BRN plot shows that when convection initiated wind shear at Lamont was too weak for the available CAPE to form supercells. As time progressed, CAPE dropped and shear increased so that more typical values of BRN were found as the towering cumulus near Lamont was developing into a supercell.

All available observation sites show a near doubling of EHI in the hour before tornadogenesis. However, changes of this magnitude are not unique to that time period; the high variability in shear parameters creates EHI and BRN values with large variation.

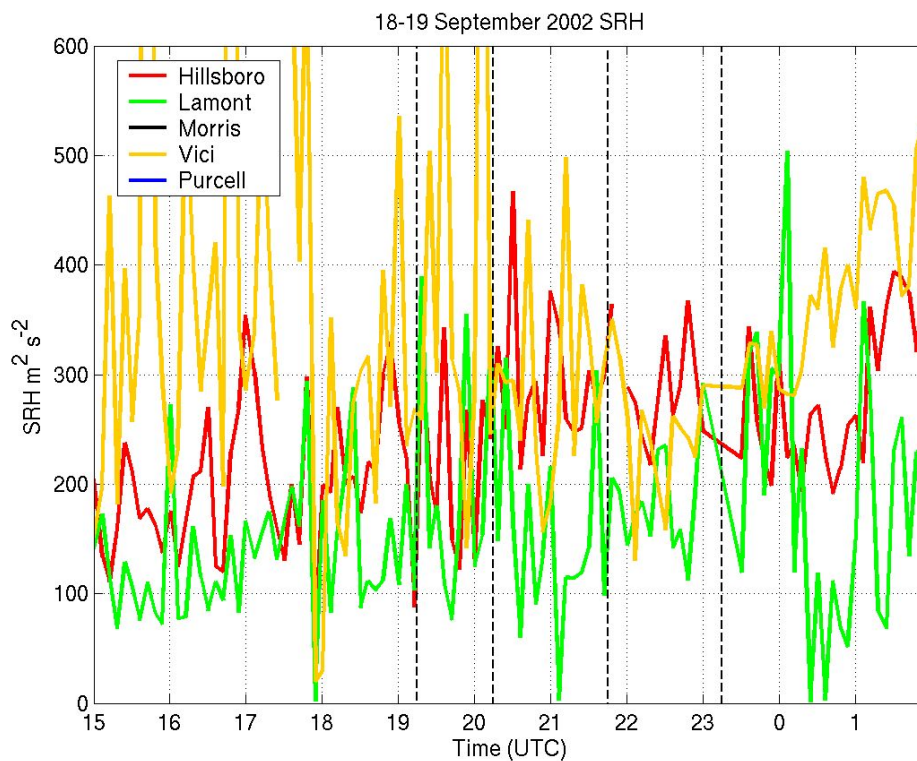


Figure 6.20: As in Figure 6.16, but for SRH as measured by wind profiler.

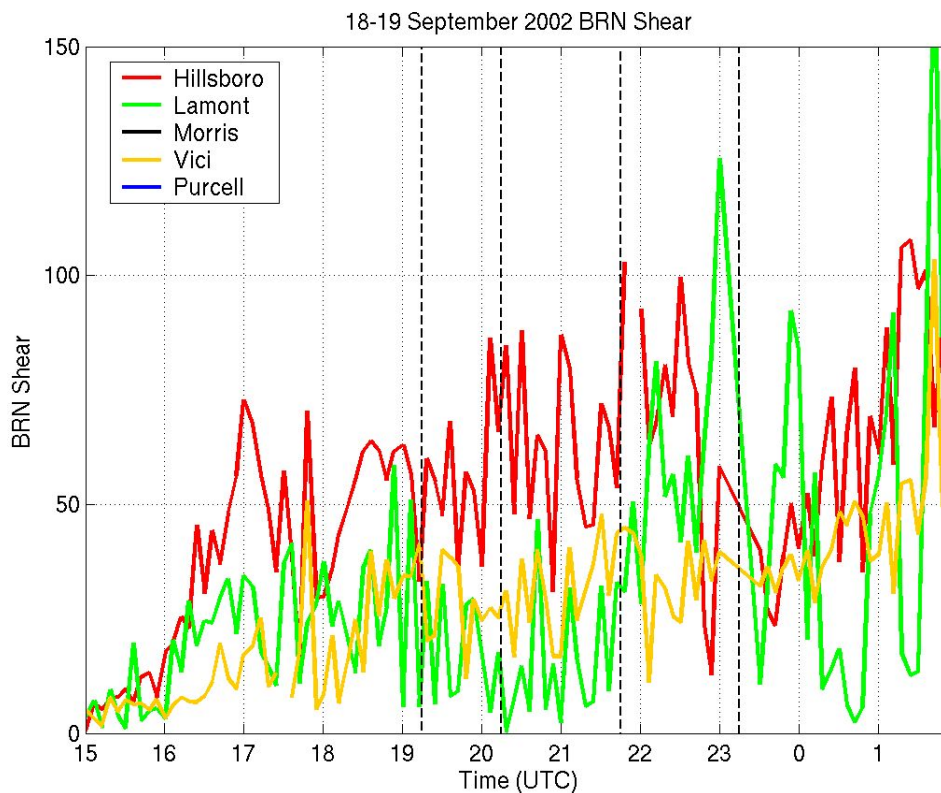


Figure 6.21: As in Figure 6.16, but for BRN shear as measured by wind profiler.

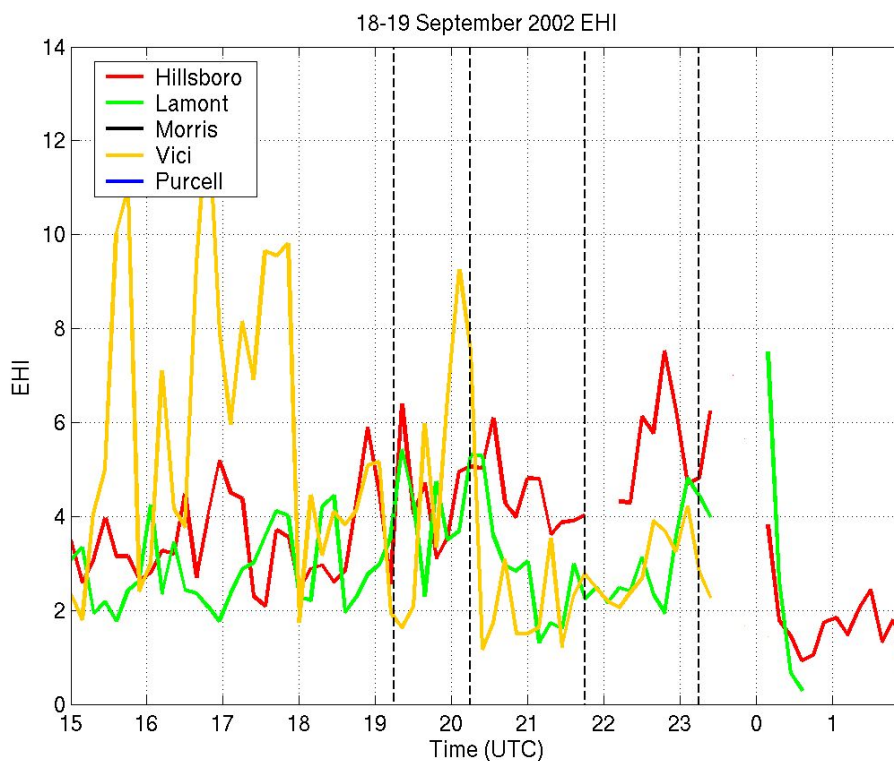


Figure 6.22: As in Figure 6.16, but for EHI as measured by AERI and wind profiler.

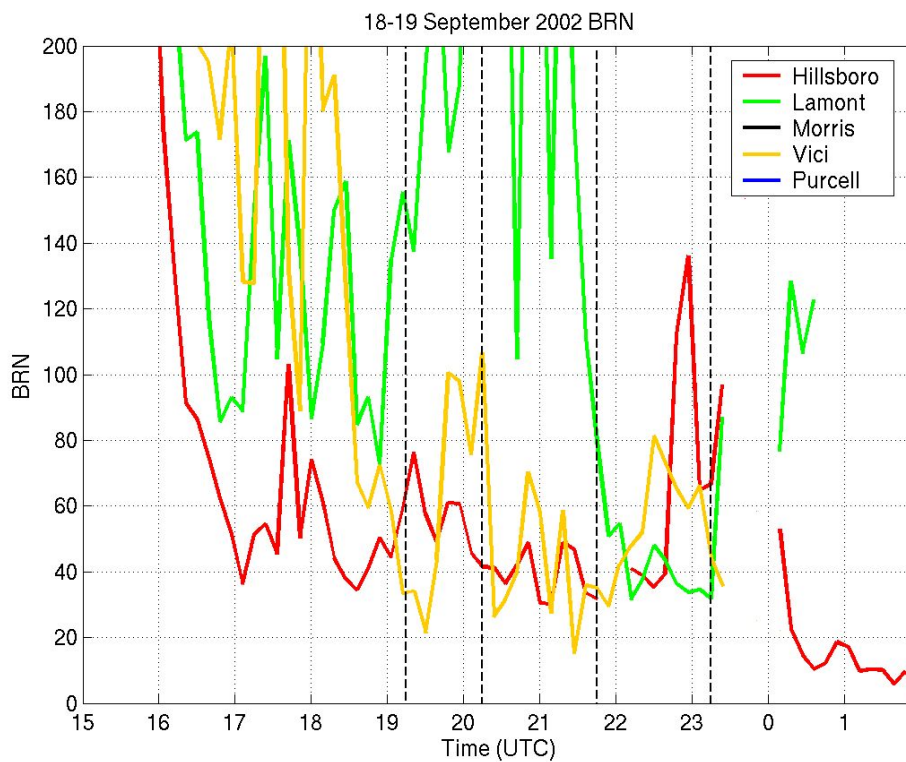


Figure 6.23: As in Figure 6.16, but for BRN as measured by AERI and wind profiler.

C. Comparisons

These two cases are drastically different. The first was a widespread outbreak of destructive tornadoes that caused hundreds of injuries and hundreds of thousands of dollars in damage. The second was a large outbreak of supercells that formed only two weak, short-lived tornadoes that caused no significant damage. The first case had substantially larger instability, greater shear, longer-lived storms, and occurred earlier in the day than the second case.

Still, there are common threads between these events. The two cases each had significant surface moisture in the pre-convective environment. Both initiated over western Oklahoma, where an advancing boundary propagated through air where convection was not as inhibited as it had been earlier in the day. Both had a balance between shear and instability that was conducive to supercell development throughout the entire experiment domain. Each shows large amounts of variability in convective indices (especially in the kinematic indices) from one time to the next and from location to location. Similar trends, especially the rapid loss of CIN, were found by Feltz and Mecikalski (2002), who used AERI retrievals to diagnose conditions associated with the 3-4 May 1999 tornado outbreak in central Oklahoma.

From dryline structure to inhibition quantities, both case studies present observations and changes that cannot be resolved with the spatial and temporal resolution of the existing rawinsonde network. It is in the domain of operational nowcasting that AERI and NPN observations can provide great benefit to the general public.

VII. Conclusions

The destructive and deadly nature of severe weather has inspired efforts to develop technologies and techniques that can better pinpoint the future time and position of specific phenomena like tornadoes and hail. While the rawinsonde has traditionally been the instrument of choice for measuring the thermodynamic and kinematic profile of the atmosphere, retrieved thermodynamic profiles from the Atmospheric Emitted Radiance Interferometer (AERI) when combined with wind profilers from the NOAA Profiler Network (NPN) provide the similar observations as rawinsondes with far better temporal resolution.

With AERI collocated with NPN at five sites in the southern Great Plains of the United States for five years, a rich dataset of atmospheric conditions associated with a variety of weather phenomena was collected. These observations were used to generate an assortment of operational convective indices used by forecasters to ascertain the instability of the atmosphere and the possible severe weather that may ensue. Climatologies of these indices for tornadic storms were calculated spanning the five years and categorized by the pre-storm to the post-storm environments.

In general, these climatologies indicate that atmospheric instability reached a peak about an hour before tornadogenesis, while wind shear remained relatively constant throughout the pre-storm period. After tornadogenesis, instability while the instability had lessened, sufficient quantities remained for continued support of storms. However, new storms rarely formed in these environments due to an increase in CIN and a lack of further lifting mechanisms.

Shear increased greatly a few hours after initial tornado development. This seems contrary to typical storm observations, in which discrete supercells merge together to form large non-rotating mesoscale convective systems (MCS) as shear decreases. However, MCS formation is usually several hours and hundreds of kilometers away from the time and location of initial tornado formation. If a storm examined in this study evolved into an MCS, it did so well outside of the experiment domain. Since most of the tornadoes in this study formed in the late afternoon, the large increase in shear a few hours after initial tornado formation could be due to boundary layer decoupling and low-level jet formation in the quiescent conditions following the storm.

Case studies show that there is little observation-to-observation variability in the retrievals of thermodynamic indices when compared to the retrieval of kinematic indices. This is likely due to the short-term variability of the atmosphere itself rather than due to instrument noise; changes in wind are far more rapid and chaotic than changes in temperature.

The individual case studies show changes happening much more rapidly than the climatologies reflect. This is a function of the varying times at which these changes occur ahead of convective initiation and tornadogenesis. If CIN decreases quickly between one and three hours ahead of convective initiation, for example, and convective initiation occurs at a varying time ahead of tornadogenesis, then the resulting median will show a far more gradual change ahead of tornadogenesis than the case studies showed.

Neither the spatial nor the temporal resolution of the existing synoptic rawinsonde network is adequate to capture the small-scale changes occurring in the atmosphere. With

observation-to-observation and site-to-site variability, the current in situ observations are not enough to give an accurate picture of the atmosphere to forecasters and modelers. Traditional convective indices developed from these rawinsonde-derived profiles do not have the high-temporal resolution that the combined AERI/NPN profiles provide. When coupled with the fact that individual cases are highly different from one another, no readily-identifiable signature was found that clearly delineates tornadic storms from non-tornadic ones.

However, combined retrievals from AERI and NPN do show promise in discriminating between environments that are likely to produce one type of storm over the other. New indices that utilize rates of change of convective indices could be developed to further utilize the wealth of data recorded by these combined instrument networks.

AERI and NPN were each developed separately to fulfill an individual purpose. Together, these two instruments provide data that is extremely useful to operational forecasters. This thesis has presented just a few of the ways in which combined thermodynamic and kinematic remotely-sensed profiles can be used to further the understanding of severe weather. If the AERI and profiler network were expanded to include more locations, not only could more truths about severe weather be uncovered, but more lives could be saved through more accurate forecasts and improved lead times.

References

- Bedka, K., R. A. Petersen, W. F. Feltz, C. S. Velden, and J. R. Mecikalski, 2006: Statistical relationships between satellite-derived atmospheric motion vector, rawinsonde, and NOAA Wind Profiler Network observations. Preprints, *7th Int'l Symp. on Tropospheric Profiling*, Boulder, CO, National Center for Atmospheric Research.
- Benjamin, S.G., K. A. Brewster, R. Brümmer, B. F. Jewett, T. W. Schlatter, T. L. Smith, and P. A. Stamus, 1991: An isentropic three-hourly data assimilation system using ACARS aircraft observations. *Mon. Wea. Rev.*, **119**, 888-906.
- , J. M. Brown, K. J. Brundage, B. E. Schwartz, T. G. Smirnova, and T. L. Smith, 1998: The operational RUC-2. Preprints, *16th Conf. on Weather Analysis and Forecasting*, Phoenix, AZ, Amer. Meteor. Soc., 249–252.
- , B. E. Schwartz, E. J. Szoke, and S. E. Koch, 2004: The value of wind profiler data in U.S. weather forecasting. *Bull. Amer. Meteor. Soc.*, **85**, 1871-1886.
- Brooks, H. E., C. A. Doswell III, and J. Cooper, 1994: On the environments of tornadic and nontornadic mesocyclones. *Wea. Forecasting*, **9**, 606-618.
- Chadwick, R. B. and N. Hassel, 1987: Profiler: The next generation surface-based atmospheric sounding system. Preprints, *3rd Int'l Conf on Interactive Information and Processing Systems for Meteorology*. New Orleans, LA, Amer. Meteor. Soc., 15-21.
- Changnon, S. A. and G. J. D. Hewings, 2001: Losses from weather extremes in the United States. *Nat. Hazards*, **2**, 113-123.
- David, C. L. and J. S. Smith, 1971: An evaluation of seven stability indices as predictors of severe thunderstorms and tornadoes. Preprints, *7th Conf. on Severe Local Storms*, Kansas City, MO. Amer. Meteor. Soc., 105-109.
- Davies, J. M., 1993a: Hourly helicity, instability, and EHI in forecasting supercell tornadoes. *17th Conf. on Severe Local Storms*, St. Louis, MO. Amer. Meteor. Soc., 107-111.
- , 1993b: Wind and instability parameters associated with supercell and non-supercell tornado events in the southern high plains. *17th Conf. on Severe Local Storms*, St. Louis, MO. Amer. Meteor. Soc., 51-55.

- and R. H. Johns, 1993: Some wind and instability parameters associated with strong and violent tornadoes: Part I: Windshear and helicity. *The Tornado: Its Structure, Dynamics, Prediction, and Hazards, Geophys. Monogr.*, No. 79, Amer. Geophys. Union, 573-582.
- , 2004: Estimations of CIN and LFC associated with tornadic and nontornadic supercells. *Wea. Forecasting.*, **19**, 714-726.
- Davies-Jones, R. P., D. Burgess, and M. Foster, 1990: Test of helicity as a tornado forecast parameter. Preprints, *16th Conf. on Severe Local Storms*, Kananaskis Park, AB, Canada. Amer. Meteor. Soc., 588-592.
- , R. J. Trapp, and H. B. Bluestein, 2001. Tornadoes and tornadic storms. *Severe Convective Storms, Meteor. Monogr.*, No. 50, Amer. Meteor. Soc., 167-221.
- Doswell III, C. A., 1996: On convective indices and sounding classification. Preprints, *5th Australian Severe Thunderstorm Conference*, Avoca Beach, New South Wales, Australia. Bureau of Meteor. pp. 7-12.
- , 2001: Severe convective storms--An overview. *Severe Convective Storms, Meteor. Monogr.*, No. 50, Amer. Meteor. Soc., 1-26.
- Doviak, R. J. and D. S. Zrnic, 1993: *Doppler Radar and Weather Observations*. 2nd ed. Academic Press. 562 pp.
- Eklund, W. L., D. A. Carter, and B. B. Balsley, 1979: Continuous measurement of upper atmospheric winds and turbulence using a VHF radar: Preliminary results. *J. Atmos. Terr. Phys.*, **41**, 983-984.
- Feltz, W. F. , W. L. Smith, R. O. Knuteson, H. E. Revercomb, H. M. Woolf and H. B. Howell, 1998: Meteorological applications of temperature and water vapor retrievals from the ground-based Atmospheric Emitted Radiance Interferometer (AERI). *J. Appl. Meteor.*, **37**, 857-875.
- and J. R. Mecikalski, 2002: Monitoring high-temporal-resolution convective stability indices using the ground-based Atmospheric Emitted Radiance Interferometer (AERI) during the 3 May 1999 Oklahoma-Kansas tornado outbreak. *Wea. Forecasting*, **17**, 445-455.

- , W.L. Smith, H. B. Howell, R. O. Knuteson, H. Woolf, and H. E. Revercomb, 2003: Near-continuous profiling of temperature, moisture, and atmospheric stability using the Atmospheric Emitted Radiance Interferometer (AERI). *J. Appl. Meteor.*, **42**, 584-597.
- , H. B. Howell, R. O. Knuteson, H. M. Woolf, D. D. Turner, R. Mahon, T. D. Halther, and W. L. Smith, 2005: Retrieving temperature and moisture profiles from AERI radiance observations: AERIPROF value-added product technical description. DOE-ARM technical report TR-066. Available: http://www.arm.gov/publications/tech_reports/arm-tr-066.pdf
- Galway, J. G., 1956: The lifted index as a predictor of latent instability. *Bull. Amer. Meteor. Soc.*, **37**, 528-529.
- Golding, B. W., 2003: Quantitative precipitation forecasting in the UK. *J. Hydrol.* **239**, 286-305.
- Hamill, T. M., R. S. Schneider, H E. Brooks, G. S. Forbes, H. B. Bluestein, M. Steinberg, D. Meléndez, and R. M. Dole, 2005: The May 2003 extended tornado outbreak. *Bull. Amer. Meteor. Soc.*, **86**, 531-542.
- Hart, J. A., 1993. SVRLOT: A new method of accessing and manipulating the NCCFC severe weather database. *17th Conf. on Severe Local Storms*, St. Louis, MO. Amer. Meteor. Soc., 40-41.
- and W.D. Korotky, 1991: The SHARP Workstation v1.50: A Skew T/Hodograph Analysis and Research Program for the IBM and compatible PC. 30 pp.
- Knuteson, R. O., H. E. Revercomb, F. A. Best, N. C. Ciganovich, R. G. Dedecker, T. P. Dirks, S. C. Ellington, W. F. Feltz, R. K. Garcia, H. B. Howell, W. L. Smith, J. F. Short, and D. C. Tobin, 2004a: Atmospheric Emitted Radiance Interferometer. Part I: Instrument design. *J. Atmos. Oceanic Tehnol.*, **21**, 1763-1776.
- , ——, ——, ——, ——, ——, ——, ——, ——, ——, ——, ——, ——, 2004b: Atmospheric Emitted Radiance Interferometer. Part II: Instrument performance. *J. Atmos. Oceanic Tehnol.*, **21**, 1777-1789.
- Menzel, W. P., F. C. Holt, T. J. Schmit, R. M. Aune, A. J. Schreiner, G. S. Wade and D. G. Gray. 1998: Application of GOES-8/9 Soundings to Weather Forecasting and Nowcasting. *Bull. Amer. Meteor. Soc.*, **79**, 2059–2077

- Miller, R. C., 1972: Notes on analysis and severe storm forecasting procedures of the Air Force Global Weather Central. Technical Report 200, Air Weather Service, United States Air Force, 190 pp. [NTIS AD744042]
- Moller, A. R., 2003. Severe local storms forecasting. *Severe Convective Storms, Meteor. Monogr.*, No. 50, Amer. Meteor. Soc., 433-480.
- Moncrieff, M. W. and J. S. A. Green, 1972: The propagation and transfer properties of steady convective overturning in shear. *Quart. J. Roy. Meteor. Soc.*, **98**, 336-352.
- National Climatic Data Center, 2003a: Storm Data: September 2002. 154 pp.
- , 2003b: Storm Data: May 2003. 462 pp.
- National Weather Service, 2003: Record Tornado Outbreaks of May 4-10 2003. NWS Service Assessment. 41 pp.
- Rasmussen, E. N. and D. O. Blanchard, 1998: A baseline climatology of sounding-derived supercell and tornado forecast parameters. *Wea. Forecasting*, **13**, 1148-1164.
- Rodgers, C. D., 2000: *Inverse Methods for Atmospheric Sounding: Theory and Practice*. World Scientific. 238 pp.
- Schultz, P., 1989: Relationships of several stability indices to convective weather events in northeast Colorado. *Wea. Forecasting*, **4**, 73-80.
- Showalter, A. K., 1953: A stability index for thunderstorm forecasting. *Bull. Amer. Meteor. Soc.*, **34**, 250-252.
- Smith, W. L., 1970: Iterative solution of the radiative transfer equation for the temperature and absorbing gas profile of an atmosphere. *App. Opt.*, **9**, 1993-1999.
- , W. F. Feltz, R. O. Knuteson, H. E. Revercomb, H. M. Woolf, and H. B. Howell, 1999: The retrieval of planetary boundary layer structure using ground-based infrared spectral radiance measurements. *J. Atmos. Oceanic Tehnol.*, **16**, 323-333.
- Stokes, G. M. and S. E. Schwartz, 1994: The Atmospheric Radiation Measurement (ARM) program: Programmatic background and design of the cloud and radiation test bed. *Bull. Amer. Meteor. Soc.*, **75**, 1201-1221.
- Storm Prediction Center, 2005: SeverePlot Version 2. Software available: www.spc.noaa.gov/software/svrplot2/

- Strauch, R. G., D. A. Merritt, K. P. Moran, K. B. Earnshaw, and J. D. van de Kamp, 1984: The Colorado wind-profiling network. *J. Atmos. Oceanic Tehnol.*, **1**, 37-49.
- Trapp, R. J., S. A. Tessendorf, E. S. Godfrey, and H. E. Brooks, 2005: Tornadoes from squall lines and bow echoes. Part I: Climatological distribution. *Wea. Forecasting*, **20**, 23-34.
- Turner, D. D., W. F. Feltz, and R. A. Ferrare, 2000: Continuous water vapor profiles from operational ground-based active and passive remote sensors. *Bull. Amer. Meteor. Soc.*, **81**, 1301-1317.
- United States Census Bureau, 1995: *Statistical Abstract of the United States 1995: The National Data Book*. United States Department of Commerce. 989 pp.
- , 2006: *Statistical Abstract of the United States 2006: The National Data Book*. United States Department of Commerce. 1023 pp.
- van de Kamp, 1988: *Wind Profiler Training Manual Number One: Principles of Wind Profiler Operation*. Office of Meteorology, National Weather Service. 34 pp.
- Weisman M. L. and J. B. Klemp, 1982: The dependence of numerically simulated convective storms on vertical wind shear and buoyancy. *Mon. Wea. Rev.*, **110**, 504-520.